Design and Radiometric Modeling of a Portable EEM Fluorescence Sensor for ppb-Level Detection of Pesticide Mixtures in Water

Nathan Holterhoff

A thesis
submitted in partial fulfillment of the
requirements for the degree of

Master of Science

University of Washington
2025

Committee:
Alexander Mamishev
Sep Makhsous

Program Authorized to Offer Degree:
Electrical and Computer Engineering

University of Washington

Abstract

Design and Radiometric Modeling of a Portable EEM Fluorescence Sensor for ppb-Level Detection of Pesticide Mixtures in Water

Nathan Holterhoff

Chair of the Supervisory Committee:
Alexander Mamishev
Department of Electrical and Computer Engineering

According to the U.S. Geological Survey (USGS), pesticide contamination of American waters is widespread, with typical samples containing mixtures of 10 to 20 active compounds. Recent studies show that agricultural runoff and seasonal application patterns are two of the most common sources of this contamination. Environmental monitoring studies help improve understanding of the distribution and persistence of pesticides in natural water systems. Enhanced detection tools are critical for environmental monitoring studies that target data collection and the analysis of water quality data. Traditional pesticide measurement methods include solvent extraction and chromatographic separation, which introduce problems such as: 1) high cost per sample, 2) slow turnaround time, and 3) limited suitability for field deployment. Recent advancements in fluorescence spectroscopy have allowed for the development of various portable measurement techniques in different applications. However, environmental agencies are still using laboratory-based analysis rather than portable optical measurement tools, which demonstrates that there is significant room for improvement in this field. The detection of pesticides using excitation-emission matrix (EEM) fluorescence requires accurate photon throughput calculation using component-based or radiometric modeling techniques. This thesis is a study of the design, modeling, and validation of an EEM fluorescence system based on multi-wavelength excitation theory. The system was designed, modeled, and evaluated in pesticide detection applications using three representative compounds: zeta-cypermethrin, myclobutanil, and glyphosate. The compounds were tested at five concentration levels to characterize the system across different detection scenarios. When compared to model predictions, the experimental results showed detection limits of 10-100 ppb for strongly fluorescent pesticides, approximately one order of magnitude above predicted values due to lower LED power than modeled. Based on the results and validation from the radiometric model, the use of compact EEM fluorescence systems in portable applications has potential to improve the frequency and cost-effectiveness of pesticide screening.

TABLE OF CONTENTS

LIST OF FIGURES

LIST OF TABLES

ACKNOWLEDGEMENTS

Over the course of my undergraduate and graduate studies, I have been blessed to have the opportunity to conduct my research under the direction of Professor Alexander Mamishev, director of the Sensors, Energy, and Automation Laboratory (SEAL) at the University of Washington's Department of Electrical and Computer Engineering. I would like to thank Professor Mamishev for consistently pushing me to deliver my best work, for guiding my research in both theoretical and applied directions, and for supporting my interest. I am equally grateful to Professor Igor Novosselov in the Department of Mechanical Engineering, who first introduced me to this research direction and gave me the opportunity, resources, and encouragement to collaborate with his team. These experiences expanded my perspective on sensor systems and their environmental applications.

I would also like to express my sincere gratitude to my thesis committee members, Dr. Sep Makhsous and Dr. Rania Hussein, for their contributions of advice, feedback, and time throughout this process. Additionally, I would like to thank my family and friends for their steadfast support and encouragement throughout my academic journey.

DEDICATION

This Thesis is dedicated to my wife, Elina Day-Holterhoff, and parents, Paul and Janice Holterhoff

Chapter 1. INTRODUCTION

1.1 PESTICIDE MONITORING REQUIREMENTS IN U.S. SURFACE AND AGRICULTURAL WATERS

Pesticides are a steady presence in U.S. rivers and streams. According to the U.S. Geological Survey (USGS), a typical sample includes about 17 different pesticides and detections were recorded at every one of the 74 long-term sites in the latest five-year survey [1]. Taken together, those mixtures pushed concentrations above Environmental Protection Agency (EPA) aquatic-life benchmarks at more than four out of five sites, even where single chemicals tested low [1]. California's monitoring tells the same story, with imidacloprid in 86 percent and bifenthrin in 74 percent of urban-runoff samples, plus 21 other insecticides [2]. Globally, the scale is large as well, with farms applying roughly 5.6 billion pounds of pesticides each year [3].

The scale of inputs that drive these detections is enormous and it has stayed large for nearly three decades. EPA and USGS both report about 1 billion pounds of active ingredients applied each year [4, 5]. Herbicides account for roughly half. Insecticides, led by neonicotinoids and pyrethroids, pose much of the near-term threat to aquatic life [4]. Monitoring needs to follow the calendar farmers use. During or a few days after planting or major rain, stream concentrations often spike and then fade. These peaks are often missed during monthly sampling [6]. This motivates a sensor approach that can watch the rise and fall in real time and at reasonable cost.

1.2 CURRENT FEDERAL HEALTH AND ECOLOGICAL STANDARDS OF PESTICIDES

What counts as "safe enough" in water? In the United States, parts-per-billion limits answer that for individual pesticides. The National Primary Drinking Water Regulations from the EPA set atrazine at 3 ppb, glyphosate at 700 ppb, and 16 other pesticides at similarly low levels [7]. Additionally, the EPA additionally publishes numerous reports and standards for acceptable levels of pesticides. The June 2025 Aquatic-Life Benchmarks provided acute or chronic thresholds for 776 parent compounds [8]. Where no federal maximum level exists, the EPA posts Human-Health Benchmarks for Pesticides, which are non-enforceable guidance, that now cover 430 active ingredients [9]. For a global perspective, the World Health Organization lists guidance for pesticides that still appear occasionally in U.S. systems [10].

Table 1-1: Federal Health and Ecological Standards. U.S. regulators set ppb-level thresholds to protect both human consumers and aquatic life.

Program	Example pesticide	Limit (ppb)	Matrix
EPA National Primary Drinking Water Regulations	Atrazine	3	Finished drinking water
EPA National Primary Drinking Water Regulations	Glyphosate	700	Finished drinking water
EPA Aquatic-Life Benchmarks (Jun 2025)	Imidacloprid (chronic, invertebrates)	0.01	Surface water
EPA Human-Health Benchmarks (2021)	Carbaryl	0.2	Source water
WHO Guideline (for comparison)	Dichlorvos	20	Drinking water

While these regulations are meant to protect the general public, they are often violated. A 2025 investigative synthesis of Safe Drinking Water Act compliance by the EWG Tap-Water Database, a cleaned, publicly searchable extract of the EPA's Safe Drinking Water Information System, found atrazine above its health-based benchmark in 479 public-water systems that collectively serve 3 million people [11]. A few misses in large systems can touch a lot of people. Food testing tells a similar story. The Food and Drug Administration Fiscal Year 2022 Pesticide Residue Monitoring Program report had analyzed 3,030 food samples across the US and recorded overall compliance above 90%. They still flagged just under 10% of samples for violations that required regulatory action [12].

1.3 WHY SOLUTION-PHASE EEM

Due to the complex and pervasive use of pesticide, a rapid detection and quantification tool is needed [13]. In the goal of developing a portable pesticide detection device, this thesis will examine solution-phase EEM fluorescence. Solution-phase EEM fluorescence excites a water sample at dozens of narrow UV–visible wavelengths and records a full emission spectrum at each point, yielding a three-dimensional cube whose diagonal ridges act as chemical fingerprints [14-16]. Recent excitation-emission studies indicate that organophosphates, carbamates, pyrethroids, neonicotinoids and triazines possess principal excitation bands between 230 nm and 360 nm, with Stokes shifts ranging from 35 nm to 140 nm across representative compounds [17]. The span is large enough that individual compounds generate quasi-orthogonal "fingerprints" inside a single EEM cube, allowing mixture resolution with multi-way calibration.

1.4 CONSTRAINTS AND ADVANTAGES OF PORTABLE EEMS

In order to make portable EEM possible, existing systems need to be miniaturized. Recent advances in LEDs and miniature spectrometers the sensitivity needed for low PPB detection practical outside the lab. Deep-UV LED arrays (250–405 nm) now deliver > 1 mW optical power per die that are able to replace bulky xenon lamps and enable battery operation for current detection methods [18]. On the detector side, Hamamatsu's fingertip-sized C12880MA spectrometer measures 20 × 12 × 10 mm, weighs 5 g, and covers 340–850 nm with electronic-shutter synchronization for under $150 BOM cost [19]. Using these or similar parts, a 2023 research prototype achieved a single wavelength fluorometer while drawing < 3 W and costing < $500 [20].

Equally important is the information layer that turns spectra into concentrations. Classic multi-way regression already delivers ppb-scale quantification: an N-way partial least-squares (N-PLS) model built on EEM cubes determined carbaryl and chlorothalonil in natural water with a root-mean-square error of prediction (RMSEP) of 0.5 $\mu g\ L^{-1}$ [21]. While we are seeking to build a new EEM system, a few portable EEM systems already exist and meet EPA aquatic-life benchmarks for pesticides (imidacloprid (0.5 ppb)) when paired with high-yield supramolecular probes [22, 23]. In further studies, third-order calibration methods, alternating quadrilinear decomposition, applied to apple-wash samples further improve selectivity incorporating pH or temperature data [24].

The practical contrast with today's regulatory workflow is stark. EPA Method 1699 stipulates solvent extraction, multi-hour high-resolution GC/HRMS analysis and strict quality-control steps that drive per-sample costs well above $200 and turnaround times into days [25, 26].

Commercial laboratories advertise \$515 for a 7- to 9-day multi-residue screen, underscoring the financial barrier to dense temporal sampling [27]. Table 1-2 summarizes these differences.

Table 1-2: Comparison of LC-MS/MS to Solution-phase EEM Fluorescence

Attribute	LC-MS/MS (current standard)	Solution-phase EEM Fluorescence
Sample prep	Extraction, cleanup, derivatization	None (direct aqueous or filtered extract)
Acquisition time	20–45 min chromatogram	< 60 s full EEM cube
Per-sample cost	\$200–\$400 (labor & consumables)	< \$2 (LED power & amortized hardware)
Field deployable?	No	Yes (handheld prototypes < 500 g)

Data sources: LC-MS/MS workflow analysis [28]; portable EEM prototypes [18, 29].

1.5 CENTRAL RESEARCH GOALS

The primary aim of this thesis is to produce a blueprint and model for the optical design of a handheld, solution-phase excitation–emission-matrix (EEM) fluorescence sensor that can detect the pesticide mixtures documented by USGS, a median of 17 compounds per sample nationwide, at or below the 10 ppb levels implicit in EPA’s newest aquatic-life benchmarks for 776 chemicals with a signal-to-noise ratio of at least 3 [8, 30]. Achieving that end goal demands an integrated treatment of optics, electronics, and data analytics. Meeting these thresholds, verified through first-principles radiometry will constitute a successful optical model.

Chapter 2. LITERATURE REVIEW

Chapter 2 serves as a summary of the research performed in understanding the detection of pesticides that informed the current optical system described in Chapters 3 and beyond. While some of the literature is beyond the scope of Chapters 3-6, these resources directly influenced the choice to study fluorescence detection of pesticides over other methods and will guide future modifications and additions to the system in coming years.

2.1 PESTICIDE CLASSES & PHOTOPHYSICS

Modern U.S. pest-management depends on five structural families: organophosphates, carbamates, pyrethroids, neonicotinoids, and triazines. These structures together account for roughly half of the one-billion-pound annual domestic pesticide use discussed in Chapter 1 [4, 31]. Multiple reviews systematized the photophysics of more than 72 parent compounds from these families, showing that their lowest-energy $\pi \rightarrow \pi^*$ or $n \rightarrow \pi^*$ transitions cluster between 225 nm (e.g., dichlorvos, parathion) and 365 nm (e.g., bifenthrin, cypermethrin) and that the resulting Stokes shifts span ≈ 40–140 nm, providing ample spectral room for excitation–emission-matrix (EEM) discrimination [32, 33]. Reported quantum yields Φ_f vary by two orders of magnitude from < 0.01 for glyphosate, whose phosphonate group lacks an extended conjugation system, to ≈ 0.25 for the carbamate insecticide carbaryl, explaining why analytical sensitivity is compound-specific [34-37].

In the field and during sampling, Natural organic matter (NOM) and dissolved inorganics complicate the idealized behavior of these pesticides. These contaminants absorb photon energy and quench fluorescence of the targeted pesticides. A 2024 study of river-water (using atrazine as the target) reported that NOM significantly inhibited atrazine. This was mainly due to photodegradation due to inner-filter effects and modulation of photochemically produced reactive intermediates [38]. Similar studies found that ionic-strength effects (increasing NaCl from 1 mM to 100 mM) reduced the fluorescence response of a molecularly imprinted hydrogel sensor by 19%, and increasing concentrations of $CaCl_2$ induced an even stronger 30 % drop. These results show the need to correct for salinity in estuarine deployments [39]. Halide ions (Cl^-, Br^-, I^-) have also been shown to quench many aromatic fluorophores by spin-orbit coupling that accelerates intersystem crossing [40].

In addition to interference from contaminates, spectral overlap among pesticide classes decreases sensitivity: the triazine herbicide atrazine exhibits fluorescence with excitation around 290–300 nm and emission near 360–370 nm; imidacloprid's photoproducts fluoresce in a very similar range, with excitation near 330–340 nm and emission around 370–380 nm, making separation difficult [41]. Likewise, several pyrethroids have reported emission maxima in the 400–450 nm region, which coincides with the blue-emitting photoproducts of carbamate insecticides [42, 43]. As stated in Chapter 1, a median of 17 co-occurring pesticides are measured per stream sample nationwide from the USGS mixture surveys [1]. These overlaps make single-wavelength fluorometry inadequate and impractical for field use. These results motivate the decision for portable EEM and possible multi-way chemometric strategies reviewed in section 2.3.

2.2 SOLUTION-PHASE EEM INSTRUMENTATION

2.2.1 *From bench fluorimeters to field units*

Until recently, excitation–emission-matrix (EEM) spectroscopy was the province of laboratory fluorimeters built around 150-450 W xenon arc lamps, dual scanning monochromators, and 90° cuvette geometries; assemblies that weigh tens of kilograms, draw hundreds of watts, and cost well over $50k [44-46]. While existing spectrometer platforms deliver high spectral purity and results, their size, power demand, and processing time make them impractical for real-time pesticide monitoring. See chapter 1, for a summary of the current field for portable spectroscopy.

2.2.2 *LED-array fluorometers with mini-spectrometers*

Recent work in this area of research has demonstrated that EEM instrumentation can be miniaturized dramatically by replacing traditional lamp–monochromator setups with compact systems using LEDs and fingertip-sized spectrometers. For instance, López-Pérez et al. (2023) developed a portable fluorimeter under $500 that uses two LEDs (365 nm and 405 nm) and achieves ppb-level detection of standard fluorophores [19]. A follow-up MDPI study trimmed the cost further, Jechow et al. (2024) successfully deployed a sensor for near-surface water reflectance measurements in environmental settings by coupling the same spectrometer as López-Pérez et al. to an microcontroller controlled LED module and demonstrated ppb-level detection limits for five model fluorophores [20].

2.2.3 *Core detectors: Hamamatsu C12880MA vs. Hamamatsu C16767MA*

The Hamamatsu C12880MA MEMS spectrometer has been the chosen sensor for many handheld EEM prototypes. It measures 20.1 × 12.5 × 10.1 mm, weighs just 5 g, and captures the 340–850 nm range with high quantum efficiency in the visible region [47]. However, this spectrometer lacks coverage below 340 nm which limits its use for samples with deep-UV signatures. Addressing this gap, Hamamatsu now offers the C16767MA. The C16767MA is a UV-sensitive mini-spectrometer that provides deep-UV (190 nm – 440 nm) sensitivity in the same compact platform as the C12880MA [48]. This new spectrometer enables portable detection of compounds (like certain pesticides) that have emissons below 300 nm.

2.2.4 *Deep-UV LED progress*

The development of deep-ultraviolet (DUV) light-emitting diodes has increased the feasibility of portable excitation–emission matrix (EEM) devices. While UV LEDs have been around for decades, early AlGaN-based emitters were limited by poor external quantum efficiency (QE < 1 %), low output powers, short operational lifetimes (less than 100 hrs), and restricted to specialized laboratories [49]. In the last decade, steady progress in production methods and device packaging has pushed QE above 10 % at 265 nm, with some devices capable of delivering several milliwatts of stable radiant flux [50]. It is currently feasible for UV LEDs to reasonably compete with xenon arc lamps for spectroscopic applications.

To enable more complex uses, commercially available UV emitters now cover key excitation bands between 255 and 295 nm [51]. This allows targeted emission bands for triazines, carbamates, and other pesticides that absorb and emit strongly below 300 nm [51]. AlGaN-based UV LEDs now can achieve continuous operational lifetimes above 10,000 hours. This overcomes a major barrier to replacing bulky lamp systems for extended environmental use [52]. Further Flip-chip bonding, when the LED die emits light through its substrate instead of through absorbing top layers, has become a preferred configuration. Flip-chip bonding has dramatically enhanced light extraction and reduced thermal resistance [52]. Additionally, by using quartz-window or quartz for encapsulation instead of traditional epoxy housings LEDs casings absorb less energy at UV wavelengths [53].

2.2.5 *Managing signal-to-noise*

Portable EEM instruments cannot use xenon lamps and cooled PMT/CCD detectors. Instead they must use milliwatt-scale deep-UV LEDs and compact CMOS mini-spectrometers. These trades can lower photon budgets and raise noise floors. Deep-UV LED reviews document highlight still-modest radiant flux and efficiency when compared with lamp sources [51]. These results underscore the SNR penalty in current and future portable EEM devices. Recent characterizations of the Hamamatsu C12880MA mini-spectrometer in field settings likewise report higher noise relative to research-grade gear, even though the device is adequate for many environmental measurements [19]. Together, these factors make SNR management a primary design constraint for handheld EEM systems.

The dominant noise sources in miniaturized detectors are dark current and read noise. Dark current increases linearly with exposure time. This means that attempts to integrate longer to improve photon counts also increase baseline noise levels [54]. In addition, CMOS spectrometers suffer from readout-related impulse noise. This noise can obscure weak fluorescence signals if not corrected through averaging, dark-signal subtraction or other correction methods [55]. These issues are less severe in cooled CCD arrays, however, cooling might not be feasible in portable devices.

Beyond the chosen spectrometer, optical hardware design choices also effect both background light and detector artefacts and can reduce noise. Most importantly, optical baffling and band-pass filtering cab suppress stray light and Raman/side-band leakage that introduce noise into baselines in EEMs. Many method and experimental papers standardize corrections for noise (Rayleigh masking, inner-filter, Raman normalization) to control instrument- and sample-induced background [56, 57]. Additionally, synchronizing the exposures with an electronic-shuttered enabled mini-spectrometer can further limit ambient contributions without reducing sensitivity [19]. Introducing some or all of these correction methods can improve raw photon capture before any digital processing.

After minimizing hardware noise, modulation of LED drivers can lift or boost weak fluorescence out of broadband noise. In practice, Lock-in detection (LED excitation modulated at a set frequency with synchronous demodulation) has been demonstrated in compact, fixed-wavelength fluorescence detectors and in multi-channel/spectrometer-based systems [58, 59]. These modulations delivered significant SNR gains under ambient conditions. Time-domain gating is another method for suppressing prompt scatter when testing length permits [60]. Time-domain gating works by delaying the detector response so that the immediate scatter from the excitation pulse is not detected. this allows only the slower fluorescence decay to be measured. These strategies are now becoming more common in low-cost optical builds and can be translated well to portable EEM architectures.

2.2.6 *Optical geometries and sampling modes*

In all spectrometry applications, optical geometry determines what fraction of emitted photons from the sample reach the detector. With good geometry, the stray excitation or scatter from the sample does not leak into the signal. In liquid samples, 90° (orthogonal) detection is the classical choice in fluorimetry because the detector views the sample perpendicular to the excitation axis. Orthogonal positioning is cable of suppressing direct and scattered excitation with minimal computation or effort from the sampling team. NIST and IUPAC state that geometry is critical for reducing noise and spectral corrections in many of their standards and best-practices.

This is because geometry determines how inner-filter and scattering artefacts are managed before any data processing [61, 62].

In the field, recent portable water-quality devices use the 90° layout when turbidity is low. These devices are often inside compact housings or flow cells. For standards, the USGS has developed guides for field-deployable fluorometers. These details practical instrument layouts, trade of some sampling methods (in situ, cuvette vs flow cell, etc.), and quality-assurance steps (Raman normalization, blank checks) that depend on geometry and sampling mode [63]. These recommendations will and do guide the work on EEM workflows and systems intended for environmental waters.

When samples are turbid, highly absorbing, or heterogeneous (suspended sediments, food matrices, biofilms), front-face detection is commonly used to measure reflection and fluorescence [64]. By intersecting excitation and emission at the surface, front-face limits reabsorption and path-length dispersion that distort intensities in square cuvettes [65]. Recent applications show robust quantitation and classification in scattering media using front-face fluorescence, including dairy systems and fruit tissues, are capable for accurate detection in dynamic environments and provide alternative analysis for environments with high concentrations of solids and slurries [64, 65].

In practice, most miniaturized and microfluidic devices favor oblique collection angles in place of orthogonal layouts. For capillary- and chip-scale laser-induced fluorescence (LIF) devices, oblique offset detection angles curb elastic scatter and improve limits of detection while preserving a compact footprint. A recent review in Chemosensors summarizes detector placements and optical trains used in CE-LIF and microfluidic LIF. These devices were capable of sub-pM sensitivity by optimizing angle, numerical aperture, and confocal volumes [66]. Complementary work in Lab on a Chip applications shows that practical, low-cost LED/LIF stacks for on-chip assays are possible. These advances show that geometry choices depending on device type and environmental conditions are integral along with illumination, filtering, and detector selection in small form factors [67].

In order to study the fundamental photo physics of pesticides standardized radiometric models are needed. For absolute radiometric work and geometry-independent benchmarking, integrating spheres are the best option. Sphere-based photoluminescence setups are capable of capturing emission in all directions and decouple measurement from angular emission patterns. Spherical geometry spectrometry allows for measurement of absolute quantum yield and emissive-flux determinations. The BAM/Resch-Genger group has produced a widely adopted body of work on sphere configurations, pitfalls, and interlaboratory reproducibility, including recent cross-platform comparisons [68]. In the future, these setups will be the practical foundation for calibrating portable systems against lab-grade references and would greatly improve the analysis in later chapters.

Two interference affect require direct attention when design miniature and portable EEM systems. First, the primary inner-filter effect scales with absorbance at the excitation wavelength and with the effective path length set by geometry. Modern correction schemes and z-position methods extend the linearity and reduce noise of the resulting matrix without diluting the sample [69]. Second, the secondary inner-filter effect (reabsorption of emitted light) is increased in orthogonal setups at high concentration but is reduced in front-face layouts, since this system is designed for low concentrations these effects might be of little concern [70]. Using geometry-aware corrections and front-face where appropriate is now standard practice when building EEMs on difficult matrices. For clear aqueous samples and benchtop validation, 90° remains the default. For turbid or surface-dominated targets, front-face is the safer choice. For miniature flow cells and chips, oblique or confocal geometries offer strong SNR at much smaller scale. Angle in the end will be determined by the constraints of the device since all have merit and drawbacks.

2.3 CHEMOMETRIC METHODS

Reliable EEM analysis starts with correction and normalization. Standard EEM workflows start with the removal of instrument response, blank subtraction, masking of Rayleigh and Raman scatter, inner-filter correction, and normalization to the integrated water Raman signal so that intensities are comparable across samples and instruments [57]. Through decades of research, the scientists and engineers have established Raman normalization as a practical calibration step for inter-study and comparability. They showed how to correct instrument-specific response so spectra from different fluorimeters align and can be used for larger scale studies [71, 72]. Current reviews and methods papers give clear guidance on absorbance-based inner-filter correction and alternative strategies when absorbance data is limited [73].

2.3.1 *Parallel Factor Analysis*

For most workflows, Parallel Factor Analysis (PARAFAC) is traditionally the principal model for identification of compounds within EEM spectra. The original tutorial by Stedmon and Bro formalized PARAFAC for fluorescence EEMs. Building on this original framework, further study and analysis by Andersen and Bro detailed practical steps for developing models for use [74, 75]. The later tutorial review by Murphy et Al. gave best practices and provided an openly documented toolbox that implements spectral corrections and PARAFAC workflows that are used widely in environmental applications [76]. These original sources have provided common validation steps, such as split-half analysis and examination of core consistency before accepting component solutions, for identification of compounds in EEM spectra.

When targets need to be quantified in complex and interfering EEMs, second-order calibration methods expand upon PARAFAC by leveraging the full three-way structure. Olivieri et Al. demonstrated the second-order advantage by showing that PARAFAC or trilinear least-squares can recover analyte concentrations in the presence of uncalibrated and random interferents [77]. They also introduced unfolded Partial Least Squares with residual bilinearization (U-PLS/RBL) to provide more confidence in predictions. U-PLS/RBL models the remaining bilinear structure after PARAFAC unfolding and often improves prediction when trilinearity does not provide a confident result. Follow-on studies have reinforced these results and offer worked examples for fluorescence datasets with strong spectral overlap [78].

2.3.2 *Partial Least Squares*

N-way Partial Least Squares (N-PLS) provides a direct multiway regression route from EEMs to concentrations. The first order algorithm was originally published in the Journal of

Chemometrics and described the algorithm for three-way data. Subsequent work quantified prediction uncertainty and compared unfolded versus tri-PLS strategies [79]. In practice, N-PLS performs well for predictive calibration when the calibration set spans expected variability (known contaminants), while second-order methods, as PARAFAC regression or U-PLS/RBL, are preferred when unmodeled interferences will be present and the second-order advantage is needed [80].

2.3.3 *Machine-learning Models*

With the advent of AI, machine-learning models complement classical chemometrics for classification and non-linear regression. Autoencoders and convolutional neural networks have been trained directly on EEMs to predict disinfection by-product formation and classify samples. These models often outperform linear baselines when sufficient data and careful validation is available, however, the training data required is quite extensive [81, 82]. These studies also illustrate best practices for model interpretation and cross-validation to guard against overfitting. For regulatory or highly interpretable use cases, linear baselines such as PCA→PLS-DA and PARAFAC-scores→PLS are more likely to be easier to audit.

Beyond choosing the best ML models for identification, software architecture matter for reproducibility and calibration transfer across future devices and studies. The drEEM toolbox from Murphy et al. implemented response corrections. Additionally, PARAFAC routines documented in the tutorial, and the staRdom R package provides a fully open workflow for EEM preprocessing and PARAFAC with built-in validation utilities that could serve as a baseline for future system [76, 83]. This recent work also summarize optical-surrogate practice for simulated dissolved organic matter. These developments will help align preprocessing and reporting across instruments, labs, and field deployments when more deployable EEM systems are made.

2.4 OTHER PESTICIDE SENSING METHODS

2.4.1 *chromatography–mass spectrometry*

When collecting field samples, current regulatory and confirmatory analysis usually used on Liquid Chromatography-Mass Spectrometry (LC–MS) and Gas Chromatography Mass Spectrometry (GC-MS) and Quick, Easy, Cheap, Effective, Rugged, and Safe (QuEChERS) style sample prep for high-throughput, multiclass residue work from either inhouse or commerical laboratories. A recent open-access review details how tandem MS methods deliver sub-µg kg^{-1} performance across matrices and why most surveillance programs standardize on them; it also surveys LC–MS/MS and GC–MS/MS configurations in current use [84]. QuEChERS is the standard extraction/cleanup workflow from Anastassiades et al. to enable rapid analysis of a variety of compounds. These processes on now included in official guidance and AOAC methods [85, 86].

2.4.2 *Immunoassays and lateral-flow tests*

For rapid screening of target pesticides, enzyme-linked immunosorbent assay (ELISA) and lateral-flow immunoassays (LFA) can identify many organophosphates, carbamates, triazines, and neonicotinoids in food and water. However, these are usually one time use and can only identify compounds above a certain concentration. A 2022 review mapped formats, labels, and performance trade-offs for pesticide LFAs. The authors highlighted competitive assay constraints for small molecules which can reduce field usability [87]. To enhance the sensitivity and accuracy of these test, fluorescent nanoparticle can be added to strength the output. In one study, up-converting nanoparticle LFAs demonstrated detection of lower concentration levels with improved readout on portable readers [88].

2.4.3 *Electrochemical biosensors*

Electrochemical sensors: enzyme-inhibition (AChE), immunosensors, and aptamer devices, are usually low-power and compact platforms that are ideal for rapid on-site testing. An ACS ES&T Water review summarizes pesticide targets, nanomaterial transducers, and typical limits of detection across a variety of electronic sensing methods [89]. For organophosphates and carbamates, mechanism-driven acetylcholinesterase (AChE) inhibition assays are widely used and are continuing to be improved in selectivity and field robustness [90]. Recent work has also shown that electrode surfaces modified with nanomaterials like graphene, carbon nanotubes, or gold nanoparticles can enhance electron transfer and stability under field conditions possibly enabling detection of pesticides [89]. Immunosensors can also be used to detect pesticides that do not act through AChE inhibition, with monoclonal antibodies yielding detection limits in the low nanomolar range [91]. Aptamer devices provide synthetic recognition elements that are more stable than enzymes in non-ideal matrices, and they are increasingly paired with portable readout systems for multi-analyte detection [92].

2.4.4 *Surface-enhanced Raman spectroscopy*

Surface-enhanced Ramen Spectroscopy (SERS) is capable of improving portable EEM devices and achieves fast, label-free fingerprinting with μg L^{-1} to ng L^{-1} potential when substrates are well engineered. A 2024 open-access review covers nanoparticle and substrate designs of

SERS devices and identified the matrix effects and figures of merit for pesticide residues in plant-derived foods and waters [93]. Additionally, broader food-safety reviews studies confirm SERS performance and discuss the validation challenges for routine monitoring [94]. SERS may be a valuable addition to any portable EEM device especially for non florescence pesticides.

2.4.5 *Paper-based microfluidics and portable microfluidics*

Paper microfluidic devices have been used for identification of a variety of properties for centuries. These cheap devices enable colorimetric, fluorometric, or electrochemical readouts with minimal reagents and recently phone camera-based detection. Recent reviews document μPAD designs and pesticide case studies and highlight these platforms for their low-cost screening rather than confirmatory analysis [95, 96]. LFA work from above sits naturally in this space and is often integrated with paper flow layers for sample handling [87].

2.4.6 *Portable and ambient mass spectrometry*

A growing number of portable GC–MS instruments and ambient ionization MS methods are enabling confirmatory analysis in the field. In 2023, a study showed a portable GC–MS correctly identified a broad pesticide panel with high accuracy and low error. The study also outlined calibration and matrix considerations practitioners should expect outside the lab [97]. Further reviews of portable MS and ambient ionization detail the hardware constraints, ionization choices, and emerging environmental applications relevant to residues work which supports the need for a more portable solution [98, 99]. These results are promising, however, they still highlight the need for a smaller, quicker, and cheaper system.

2.5 IDENTIFIED GAPS IN THE LITERATURE

Despite recent and ongoing advances in pesticide analysis, some unresolved gaps steer and direct the work plan of this thesis. Fluorescence excitation–emission spectroscopy was efficient in the discrimination of many classes of pesticides in the laboratory setting. The majority of demonstrations, however, are made on high-performance benchtop fluorimeters with xenon lamps and scanning monochromators and highly controlled environments. They provide high-quality spectra but are conventionally not suitable for field deployment due to their power, size, and cost. Therefore, the literature is extremely scarce with reports of field-portable EEM systems with sufficient spectral fidelity for chemometric classification.

The second gap is minimal validation of low-cost instrumentation for laboratory and field use. While there are a studies that use mini spectrometers or studies of LED excitation, most of them simply publish feasibility without systematic comparison to traditional laboratory hardware. This issue adds uncertainty into how accurate these compact designs are and their ability to capture fine spectral features permitting chemometric discrimination between structurally similar pesticides.

Third, there is a lack in the chemometric modeling paradigm that can be transferred to portable fluorescence data. PARAFAC and other multiway models are largely used for decomposing dissolved organic matter EEMs, but fewer studies have employed radiometric or supervised classification models for direct use in pesticide detection. Furthermore, very few studies validate how models trained on benchtop data generalize to spectra acquired with portable equipment. This lack inhibits the transition from proof-of-concept to field-deployable analytical tools.

The purpose of this thesis is not to deliver a fully realized handheld device. Instead, I am establishing the radiometric modeling framework and demonstrating pesticide detection using low-cost benchtop instrumentation as a controlled analogue for portable systems. By focusing on radiometric corrections, spectral preprocessing, and chemometric classification with benchtop data, the critical baseline needed to translate fluorescence spectroscopy into the field will be established. These results define the performance envelope of affordable hardware, quantify the sensitivity and specificity achievable with radiometric modeling, perform simple benchtop experiments on commercially available pesticides and to set the stage for future integration into compact, LED-driven spectrometers. The long-term goal is a handheld platform capable of multi-analyte classification in real-world samples.

Chapter 3. RADIOMETRIC MODEL

3.1 INTRODUCTION

Designing a field-portable fluorescence system for pesticides requires hard trade-offs. By the nature of these portable systems, they need smaller light sources and smaller detectors to reduce cost and power demand. However, these reduction also shrink the photon budget. Classic benchtop spectrometers and fluorimeters improved sensitivity by using high-intensity broadband lamps, scanning monochromators, and low-noise detectors. They deliver excellent limits of detection but are impractical for field deployment due to scale and cost [100].

Newer Deep-UV LEDs can be compact, battery-friendly while providing excitation in the 255–295 nm region. This light range excites many pesticide chromophores, yet the radiant flux and external quantum efficiency of compact LEDs remain orders of magnitude lower than arc lamps. A comprehensive review documented typical output levels, EQE trends, and reliability improvements that bound what a handheld device can reasonably expect from LED excitation, see this study for the design of UV LEDs [51].

Miniature spectrometers set the other side of the ledger. The Hamamatsu C12880MA (≈340–850 nm) and C16767MA (≈190–440 nm, UV-enhanced) are Fingertip-sized CMOS spectrometer modules. They provide realistic collection efficiency, spectral coverage, and readout noise needed for portable builds. Their datasheet specifies package size, spectral range, and core performance attributes that are comparable to some benchtop devices and relevant to the needed responsivity and background [48].

For pesticides specifically, much of the EEM literature demonstrated multivariate analysis on relative intensities collected with benchtop instruments. This analysis leaves open the question of how far low-cost hardware can go when calibrated radiometrically. Early and subsequent studies achieved simultaneous determination of pesticides in water using EEM methods and devices with multivariate calibration or PARAFAC; related work extended second-order calibration to complex food matrices which introduced significant interference [101-103]. These studies prove spectral discriminability but never discussed the radiometric budget and optimizations that could be made to portable hardaware, which is essential for translating bench performance to LED-driven portable devices.

Miniature spectrometers set the other side of the ledger. Fingertip-sized CMOS modules such as the Hamamatsu C12880MA (≈340–850 nm) and C16767MA (≈190–440 nm, UV-enhanced) define realistic collection efficiency, spectral coverage, and readout noise for portable builds. Their official datasheet specifies package size, spectral range, and core performance attributes relevant to instrument responsivity and background [48].

In this chapter, I use a radiometric framework to connect engineering choices to analytical performance. The model below uses LED power, optical geometry, path length, sample absorbance, spectrometer responsivity, and noise to predicted signal and noise counts. From that, I estimated theoretical detection limits under practical and device driven constraints (LED drive, integration time, and averaging), and identify cost-sensitive levers, such as intensity of LEDs, required spectral resolution, and whether portable systems are capable of regulatory work. This work is not comprehensive, however, it can be used to verify result and make initial design choices.

3.2 NOTATION

Table 3-1 collects every symbol that appears in Equations 4-1 through 4-9 and describes what each stands for and the SI unit that accompanies it.

Table 3-1: Key Terms for Modeling

Symbol	Meaning	Typical Unit
P_{LED}	Electrical drive power	W
η_{e-o}	Electrical-to-optical efficiency of LED	$-$
Φ_{exc}	Excitation radiant flux leaving LED package	W

λ_{exc}	Excitation Wavelength	m
h	Planck constant, $6.636 * 10^{-34}$	J s
c	Speed of light $3.00 * 10^{8}$	$m\,s^{-1}$
f_{opt}	Geometric & Coating transmission to sample	$-$
L	Sample Path Length	m
$\epsilon(\lambda)$	Molar Absorptivity	$L\,mol^{-1}\ \ cm^{-1}$
C	Analyte concentration	$mol\,L^{-1}$
Φ_f	Fluorescence quantum yield	$-$
$\frac{\Omega}{4\pi}$	Fractional solid angel collected	$-$
τ_{opt}	Optical train transmission (lenses + filters)	$-$
$QE(\lambda)$	Detector Quantum efficiency	$-$
t_{int}	Integration time	s
N_{dark}	Dark/electronic noise electrons	e^{-}
N_{read}	Read noise (rms)	e^{-}

3.3 THEORETICAL BACKGROUND

The radiometric model estimates the photon throughput of the instrument, beginning with the LED source and ending at the detector pixel array. To see a quick flow diagram of the system, see Figure 3-1: Simplified Optical Flow Diagram. Each stage of the optical model introduces physical constraints that collectively determine achievable sensitivity and detection limits.

3.3.1 *LED output power*

The radiant flux leaving the LED package is the product of the electrical drive power and the wall-plug efficiency:

$$\Phi_{exc} = P_{LED}\eta_{e-o} \tag{3-1}$$

3.3.2 *Photon flux entering the sample*

Dividing radiant flux by the energy per photon, then applying an optical transmission factor f_{opt}, gives the excitation photon rate delivered to the cuvette:

$$\dot{N}_0 = \frac{\Phi_{exc} f_{opt}}{\frac{hc}{\lambda_{exc}}} \tag{3-2}$$

3.3.3 *Beer–Lambert law defines absorbance as*

$$A = \epsilon(\lambda_{exc})CL \tag{3-3a}$$

and the fraction of photons absorbed by analyte molecules is,

$$f_{abs} = 1 - 10^{-A} \tag{3-3b}$$

3.3.4 *Photon emission rate*

Each absorbed photon has a probability, Φ_f of being re-emitted as fluorescence, yielding,

$$\dot{N}_{emit} = \dot{N}_0 f_{abs} \Phi_f \tag{3-4}$$

3.3.5 *Optical collection*

Only a small fraction of emission is collected, defined by the solid-angle fraction $\frac{\Omega}{4\pi}$ and optical throughput τ_{opt}:

$$\dot{N}_{Coll} = \dot{N}_{emit} \frac{\Omega}{4\pi} \tau_{opt} \tag{3-5}$$

3.3.6 *Detector photoelectron rate*

The detector's quantum efficiency turns incoming photons into photoelectrons; this is the electron-arrival rate at the pixel array.

$$\dot{N}\,_{e}^{-} = \dot{N}_{coll} QE(\lambda_{em}) \tag{3-6}$$

3.3.7 *Signal and shot noise*

Multiply by integration time to get total signal charge, then take the square root for Poisson (shot) noise.

$$S = \dot{N}_{e^-} t_{int}, \sigma = \sqrt{S} \tag{3-7}$$

3.3.8 *Total noise*

Combine shot noise with fixed dark electrons and the sensor's read noise in quadrature to obtain the overall noise figure.

$$\sigma_{tot} = \sqrt{\sigma_{shot}^2 + N_{dark} + N_{read}^2} \tag{3-8}$$

3.3.9 *Signal-to-noise ratio*

The signal-to-noise ratio is defined as the signal charge over the total noise.

$$SNR = \frac{S}{\sigma_{tot}} \tag{3-9}$$

3.3.10 *Limit of detection*

Following the U.S. EPA convention, a detection is considered significant when SNR ≥ 3 (one-tailed, 99% confidence). Rearranging gives an expression for the minimum detectable concentration:

$$SNR_{LOD} \geq 3, C_{min} = \frac{\frac{3}{t_{int}}\sqrt{\sigma_{shot}^2 + N_{dark} + N_{read}^2}}{\frac{\epsilon(\lambda_{exc}) L \Phi_f F_{opt} \left(\frac{\Omega}{4\pi}\right) \tau_{opt} QE}{\frac{hc}{\lambda_{exc}}}} \tag{3-10}$$

The photon budget model (Eqs. 4-1 through 4-10) follows directly from first principles of radiometry and spectroscopy as outlined by Strojnik (2017), Harris (2015), and Lakowicz (2006) [100, 104, 105].

3.4 OPTICAL FLOW DIAGRAM

Figure 3-1 illustrates the simplified optical flow used in the radiometric model. Each block represents a physical subsystem of a standard spectroscopy setup, while the arrows correspond to the processes described by Equations (3-1) through (3-10). Beginning with the LED source, electrical drive power is converted to optical flux. This flux is collimated and directed to the sample cuvette. The analyte absorbs a fraction of the excitation light according to the Beer–Lambert law. Under this excitation, fluorescence emission occurs from the sample with probability determined by the quantum yield. A portion of the emission is collected by collection lenses and filters and then is measured by the spectrometer. The quantum efficiency and noise processes of the spectrometer determine the final signal. The microcontroller unit (MCU) processes this signal into chemometric outputs used for discrimination of the pesticide.

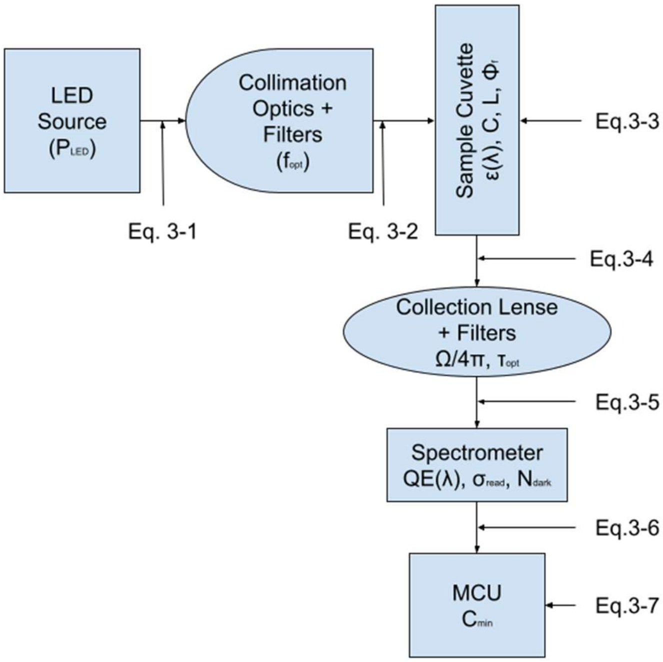

Figure 3-1: Simplified Optical Flow Diagram

3.5 MODEL ASSUMPTIONS AND LIMITATIONS

The radiometric model used above is only meant to derive some base understanding and expected response for laboratory work. It is designed to provide a tractable framework for estimating signal levels and projecting detection limits for pesticides, and not to serve as an authoritative representation, as later experiments demonstrate extreme noise. Many simplifying assumptions were made to achieve this goal. Excitation from the LEDs was treated as monochromatic, although deep-UV LEDs exhibit finite bandwidths of 10–15 nm, and there will be multiple excitation bands for every pesticide. This simplification allowed calculation of photon flux but does not capture spectral overlap with absorption of target molecules. It also does not account for the energy of emission photons, which follow a normal distribution and not a single wavelength. Emission was modeled as if arising at a single representative wavelength with a single detector quantum efficiency value, even though pesticide fluorescence is distributed across a spectral band and the spectrometer responsivity is wavelength dependent. The Beer–Lambert law was applied under the assumption of a homogeneous sample with a fixed path length and neglected scattering, turbidity, or spatial variations in analyte concentration that are present in natural waters. Optical transmission factors (lens throughput, filter efficiency, and collection solid angle) were also assumed to be constant, however, these depend on a number of factors beyond device design. Fixed quantum yields were used for glyphosate, zeta-cypermethrin, and myclobutanil, despite the fact that values for these compounds are sparse in the literature and will vary with pH, solvent, or excitation wavelength. Noise was also represented using the standard quadrature combination of shot noise, dark current, and read noise which is does not include many possible sources of noise. While this representation is widely used, it does not capture temporal drift, pixel-to-pixel variation, or stray light. The model assumes linearity across the concentration range, with signal proportional to absorbed photons.

These assumptions place many limitations on the interpretation of the work above. The most important is the lack of experimentally verified quantum yields and molar absorptivity for the three pesticides used. The reported detection limits should be used as a relative estimate that reflect the comparative detectability of weak versus strong fluorophores and not as absolute thresholds. The work also does not account for interference from environmental factors. These include quenching and spectral interference from natural organic matter, particulates, or background fluorophores. All of these factors are known to complicate detection in environmental samples. Similarly, the effects of environmental conditions, like temperature dependence of LED output or baseline drift in the spectrometer, are not included, even though they will strongly influence portable deployment. The optical path is also simplified to idealized components. Real systems include additional reflective and refractive losses. Detector performance was taken from datasheet specifications at 25 °C. In practice, dark current can rise sharply at elevated temperatures due to excitement and further reduce sensitivity. These assumptions are simplified below in Table 3-3.

Table 3-2. Assumptions used in the radiometric model and their practical implications.

Assumption	**Practical Implication**
Excitation treated as monochromatic	Real LEDs have 10–15 nm bandwidth; overlap with absorption shoulders may alter photon flux.

Homogeneous sample, fixed path length	Neglects scattering, turbidity, and gradients present in natural waters.
Constant optical transmission/collection	Ignores alignment drift, surface losses, and variations in cuvette or fiber coupling.
Fixed quantum yields	Literature values are scarce; yields vary with solvent, pH, and excitation wavelength.
Single emission wavelength for QE	Pesticide fluorescence spans bands; detector responsivity is wavelength dependent.
Noise modeled as shot + dark + read	Does not capture temporal drift, pixel nonuniformity, or stray light.
Linear Beer–Lambert response	Breaks down at high absorbance ($A > 1$) where self-absorption and reabsorption occur.
Datasheet detector specs at 25 °C	Dark current increases at higher field temperatures, reducing sensitivity.

3.6 WORKED EXAMPLE

To demonstrate the use of the radiometric model, I consider the benchtop measurements performed in a later chapter with the three pesticides: glyphosate (a phosphonate herbicide), zeta-cypermethrin (a pyrethroid insecticide), and myclobutanil (a triazole fungicide). These compounds were selected to represent different chemical classes with distinct absorption, emission properties, and commercial accessibility for benchtop verification. While more analysis is needed, these compounds are highly available to the general public for rapid analysis, which is why they were chosen for this thesis.

Precise fluorescence quantum yields (Φ_f) and molar absorptivities (ϵ) for glyphosate, zeta-cypermethrin, and myclobutanil under UV excitation are not documented in open literature and do not have definitive values. Many pesticides are documented to be weakly fluorescent with quantum yields too low for direct detection in standard setups, however, they still can possibly be detected using EEM methods [22]. Therefore, the values used here are estimated based off of readily available quantum yields, selected to reflect relative fluorescence strengths consistent with chemical expectations: glyphosate < myclobutanil < zeta-cypermethrin. These are to be experimentally verified in the future since Chapter 5 shows extreme deviations. The goal of the calculations below is to determine the SNR at 1 $\mu M\ L^{-1}$ concentration to simplify calculations. This is equivalent to about ~250 ppb, which is an acceptable mi

3.6.1 *Model inputs*

- **Excitation source:** A 280 nm deep-UV LED driven at $P_{LED} = 1.0\ W$. The wall-plug efficiency of this device is ~3%, giving an excitation flux .$\Phi_{exc} = 0.03\ W$ [51].
- **Optical train:** Collimation optics with transmission $f_{opt} = 0.6$. Path length $L = 1\ cm$. Collection solid angle fraction $\frac{\Omega}{4\pi} = 0.02$ (corresponding to NA ≈ 0.25). Optical throughput (filters + lenses) $\tau_{opt} = 0.8$.
- **Sample properties:**
    - Glyphosate: weak fluorophore, quantum yield $\Phi \approx 0.01$, molar absorptivity $\epsilon(280nm) \approx 150\ L\ mol^{-1}cm^{-1}$.

- Zeta-cypermethrin: stronger fluorophore, quantum yield $\Phi \approx 0.08$, molar absorptivity $\epsilon(280nm) \approx 12{,}000\ L\, mol^{-1} cm^{-1}$.
- Myclobutanil: intermediate strength, quantum yield $\Phi \approx 0.05$, molar absorptivity $\epsilon(280nm) \approx 4{,}000\ L\, mol^{-1} cm^{-1}$.

- **Detector:** Miniature CMOS spectrometer (Hamamatsu C16767MA). Average quantum efficiency $QE \approx 0.7$. Dark noise $N_{dark} \approx \frac{50\frac{e^-}{pixel}}{s}$. Read noise $\sigma_{read} \approx 20\ e^-$.

3.6.2 *Photon Budget Calculation*

Using Equations (4-1) through (4-5), the excitation photon flux delivered to the sample is:

$$\dot{N}_0 = \frac{0.03\ W * .6}{\frac{(6.626 \times 10^{-34} J\ s)\left(3.00 \times 10^8 \frac{m}{s}\right)}{280 \times 10^{-9}\ m}}$$

$$\dot{N}_0 \approx 2.5\ \times 10^{16} \frac{photons}{s}$$

From this flux, the absorbed fraction f_{abs} is estimated using Eq. (3-3) for each analyte at a representative concentration of 1 $\mu M\ L^{-1}$ for simplified calculations:

- Glyphosate: $A \approx 0.00015, \quad f_{abs} \approx 0.000345.$
- Zeta-cypermethrin: $A \approx 0.012, \quad f_{abs} \approx 0.0273.$
- Myclobutanil: $A \approx 0.004, \quad f_{abs} \approx 0.00917.$

Photon emission rates (Eq. 4-4) are then:

- Glyphosate: $\dot{N}_{emit} \approx 8.76\ \times 10^{10} s^{-1}.$
- Zeta-cypermethrin:$\dot{N}_{emit} \approx 5.53\ \times 10^{13} s^{-1}$

- Myclobutanil: $\dot{N}_{emit} \approx 1.16 \times 10^{13} s^{-1}$

After applying collection efficiency (Eq. 4-5), detector QE (Eq. 4-6), and integrating for $t_{int} = 1s$:

- Glyphosate: $9.81 \times 10^{8} e^{-}$.
- Zeta-cypermethrin: $6.19 \times 10^{11} e^{-}$.
- Myclobutanil: $1.30 \times 10^{11} e^{-}$.

3.6.3 *Signal-to-Noise Ratios*

Using Eqs. (3-7 to (3-9), the SNR values are estimated as:

- Glyphosate: SNR ≈ 3.1×10^{4}.
- Zeta-cypermethrin: SNR ≈ 7.9×10^{5}.
- Myclobutanil: SNR ≈ 3.6×10^{5}.

3.6.4 *Interpretation*

The worked examples above highlights the very different detection levels of pesticides. These detection levels are governed by the fluorescence quantum yield and molar absorptivity of each pesticide. Zeta-cypermethrin produces strong fluorescence and is readily detectable at trace concentrations, while glyphosate poses a much greater challenge, it is less detectable by nearly an order of magnitude. The radiometric model quantifies these trade-offs and also shows how LED output, optical efficiency, and detector noise can directly increase or decrease pesticide-specific detection limits. These results also explain why glyphosate is often considered a poor fluorophore in literature, while aromatic pesticides such as pyrethroids and triazoles are better suited to EEM-based detection.

3.7 MODEL ASSUMPTIONS AND LIMITATIONS

The radiometric model used above is only meant to derive some base understanding and expected response for laboratory work. It is designed to provide a tractable framework for estimating signal levels and projecting detection limits for pesticides, and not to serve as an authoritative representation, as later experiments demonstrate extreme noise. Many simplifying assumptions were made to achieve this goal. Excitation from the LEDs was treated as monochromatic, although deep-UV LEDs exhibit finite bandwidths of 10–15 nm, and there will be multiple excitation bands for every pesticide. This simplification allowed calculation of photon flux but does not capture spectral overlap with absorption of target molecules. It also does not account for the energy of emission photons, which follow a normal distribution and not a single wavelength. Emission was modeled as if arising at a single representative wavelength with a single detector quantum efficiency value, even though pesticide fluorescence is distributed across a spectral band and the spectrometer responsivity is wavelength dependent. The Beer–Lambert law was applied under the assumption of a homogeneous sample with a fixed path length and neglected scattering, turbidity, or spatial variations in analyte concentration that are present in natural waters. Optical transmission factors (lens throughput, filter efficiency, and collection solid angle) were also assumed to be constant, however, these depend on a number of factors beyond device design. Fixed quantum yields were used for glyphosate, zeta-cypermethrin, and myclobutanil, despite the fact that values for these compounds are sparse in the literature and will vary with pH, solvent, or excitation wavelength. Noise was also represented using the standard quadrature combination of shot noise, dark current, and read noise which is does not include many possible sources of noise. While this representation is widely used, it does not capture temporal drift, pixel-to-pixel variation, or stray light. The model assumes linearity across the concentration range, with signal proportional to absorbed photons.

These assumptions place many limitations on the interpretation of the work above. The most important is the lack of experimentally verified quantum yields and molar absorptivity for the three pesticides used. The reported detection limits should be used as a relative estimate that reflect the comparative detectability of weak versus strong fluorophores and not as absolute thresholds. The work also does not account for interference from environmental factors. These include quenching and spectral interference from natural organic matter, particulates, or background fluorophores. All of these factors are known to complicate detection in environmental samples. Similarly, the effects of environmental conditions, like temperature dependence of LED output or baseline drift in the spectrometer, are not included, even though they will strongly influence portable deployment. The optical path is also simplified to idealized components. Real systems include additional reflective and refractive losses. Detector performance was taken from datasheet specifications at 25 °C. In practice, dark current can rise sharply at elevated temperatures due to excitement and further reduce sensitivity. These assumptions are simplified below in Table 3-3.

Table 3-3. Assumptions used in the radiometric model and their practical implications.

Assumption	**Practical Implication**
Excitation treated as monochromatic	Real LEDs have 10–15 nm bandwidth; overlap with absorption shoulders may alter photon flux.

Homogeneous sample, fixed path length	Neglects scattering, turbidity, and gradients present in natural waters.
Constant optical transmission/collection	Ignores alignment drift, surface losses, and variations in cuvette or fiber coupling.
Fixed quantum yields	Literature values are scarce; yields vary with solvent, pH, and excitation wavelength.
Single emission wavelength for QE	Pesticide fluorescence spans bands; detector responsivity is wavelength dependent.
Noise modeled as shot + dark + read	Does not capture temporal drift, pixel nonuniformity, or stray light.
Linear Beer–Lambert response	Breaks down at high absorbance (A > 1) where self-absorption and reabsorption occur.
Datasheet detector specs at 25 °C	Dark current increases at higher field temperatures, reducing sensitivity.

3.8 LOCAL SENSITIVITY

In order to identify which design variables exert the strongest first-order control over signal-to-noise ratio, I performed a local sensitivity analysis on the prior model. Each lever, LED radiant flux Φ_{LED}, solid-angle fraction $\frac{\Omega}{4\pi}$, optical transmission τ_{opt}, detector quantum efficiency QE, and integration time t_{int} is changed by an infinitesimal amount, while all other variables are held fixed. The resulting partial derivatives of the SNR logarithm provided a linear "gain" that ranked the variable levers by their immediate impact on the strength of the signal. Table 3-4 lists the derivatives, their numerical values at the baseline, and the physical interpretation of each term. Because SNR scales as the square root of photon rate, the elasticities of flux, Φ_{LED}, $\frac{\Omega}{4\pi}$, τ_{opt}, and QE all collapse to 0.5, whereas the elasticity of integration time is exactly 0.5 by definition of Poisson statistics. The elasticities in Table 3-2 are calculated under the shot-noise–limited regime, where the detected photon rate dominates dark and read noise. These elasticities do not hold If detector noise or background dominates. Under this condition, all levers and integration time contribute symmetrically with coefficients of 0.5. These equal coefficients confirm that SNR responds symmetrically to proportional changes in any lever, and that downstream design effort should prioritize the most cost- or mass-efficient change rather than one with higher mathematical weight.

Table 3-4: Key Terms for Modeling

Variable	Symbol	$\partial \ln \mathrm{SNR} / \partial \ln x$	Numerical value (baseline)	Interpretation
LED optical flux	Φ_{LED}	½	0.50	Doubling LED flux raises SNR by √2
Collection solid angle	$\frac{\Omega}{4\pi}$	½	0.50	Doubling lens radius (solid angle ×4) yields ×2 SNR

Optical transmission	τ_{opt}	½	0.50	A 10 % filter loss depresses SNR by 5 %
Detector QE	QE	½	0.50	Changing from 0.40 → 0.60 QE increases SNR by 22 %
Integration time	t_{int}	½	0.50	Four-fold longer exposure doubles SNR (but costs battery)

Variables tied to the sample (molar absorptivity ε and quantum yield Φ_f,) are excluded here because they are not under optical-design control; their influence will be discussed separately.

Chapter 4. SENSITIVITY SCAN

4.1 PARAMETER SPACE DEFINITION

For the sake of space and to prevent repetitive examples, all analysis will be done using the fluorescence properties for carbaryl in since the quantum yield is extensively documented. This was chosen as it properties represent a middle ground for the fluorescence properties of many pesticides and it must be detected at an extremely low 10 ppb. Future work will be done to quantify other pesticides.

4.1.1 *Design Levers and Ranges*

Table 4-1. Design Levers and Ranges

Symbol	Physical meaning	Baseline	Min – Max used in sweeps	Rationale
Φ_{LED}	Optical radiant flux leaving UV LED (W)	0.030 W	0.005 – 0.30 W	Nichia NVSU233B and NVSU365A families deliver 5 mW at 20 mA and up to 300 mW at ≈ 1 A without forced cooling, a practical ceiling for handheld enclosures [106, 107]
$\frac{\Omega}{4\pi}$	Fractional solid angle captured by collection lens	0.010	0.002 – 0.030	UV-grade fused-silica singlets of 5–20 mm clear aperture at 15 mm working distance give this range [100, 108].
τ_{opt}	In-band transmission of filters + lenses	0.70	0.50 – 0.90	Semrock/MidOpt interference stacks transmit

				50–90 % across 330–700 nm while blocking the 270 nm pump at OD ≥ 4 [18]
QE	Detector quantum efficiency at 360 nm	0.40	0.25 – 0.55	Hamamatsu C16767MA data show 25 % (lot minimum) to >50 % (typical peak) in the UV and near UV range [109].
t_{int}	Integration time per EEM plane (s)	1 s	0.05 – 5 s	Field fluorimeters report 50 ms fast mode and 1–5 s high-sensitivity mode; longer exposures draw battery but improve SNR by √t [20].
M	Matrix factor (turbidity & self-absorption)	1.0	0.5 – 1.0	Laboratory-filtered water sets M=1; turbid runoff can halve optical throughput (~NTU > 100) per recent compensation studies [110].

4.2 MATRIX EFFECTS AND ENVIRONMENTAL ATTENUATION

Although the photon budget outlined in Chapter 3 assumes pristine optical conditions, environmental factors such as turbidity, re-absorption, and scattering reduce the number of fluorescence photons that reach the detector. These losses are summarized by a dimensionless matrix factor M in the range $0 < M \leq 1$. Values near 1 correspond to clear laboratory water, while values closer to 0.5 approximate turbid surface runoff or raw process samples.

4.3 GLOBAL SENSITIVITY AND INTERACTION ANALYSIS

Chapter 3 presented a photon-budget model that shows how several factors work together to set the detection limit: LED output, collection optics, optical transmission, detector efficiency, and exposure time. These factors multiply together in the model. But once noise and nonlinear effects were added, it became harder to see which factors mattered most. The key question was which design choices would actually improve performance. A global sensitivity analysis using Sobol variance decomposition was conducted on the detection limits to answer this. Earlier work included a local elasticity scan that looked at tiny changes near the baseline values. The Sobol approach is different. It looks at how uncertainty throughout the whole design space shows up in the final results.

First-order indices, S_i, measure how much each parameter contributes on its own. Total-effect indices, S_{Ti}, capture both main effects and interactions with other parameters. If S_i and S_{Ti} are approximately equal, the parameters work independently. A large difference between them means the parameter interacts strongly with other design choices. The model response here is the log of the detection limit in ppb, which keeps variance stable across orders of magnitude.

Background counts were set to zero, making the analysis not dependent on external factors, so the variance comes from design choices and not random noise.

This framework addresses three questions. First, which hardware parameters contribute most to sensitivity: LED radiant flux Φ_{LED}, collection solid angle $\frac{\Omega}{4\pi}$, optical throughput τ_{opt}, detector quantum efficiency (QE), or integration time t_{int}? Second, do these parameters act independently or are there trade-offs between them? For example, does LED power trade off against collection optics? Third, how do interactions change what the earlier elasticity results showed? The figures below show the S_1 and S_T indices. They rank each parameter by its effect on detection limits. They also reveal where design decisions need to be made together rather than separately.

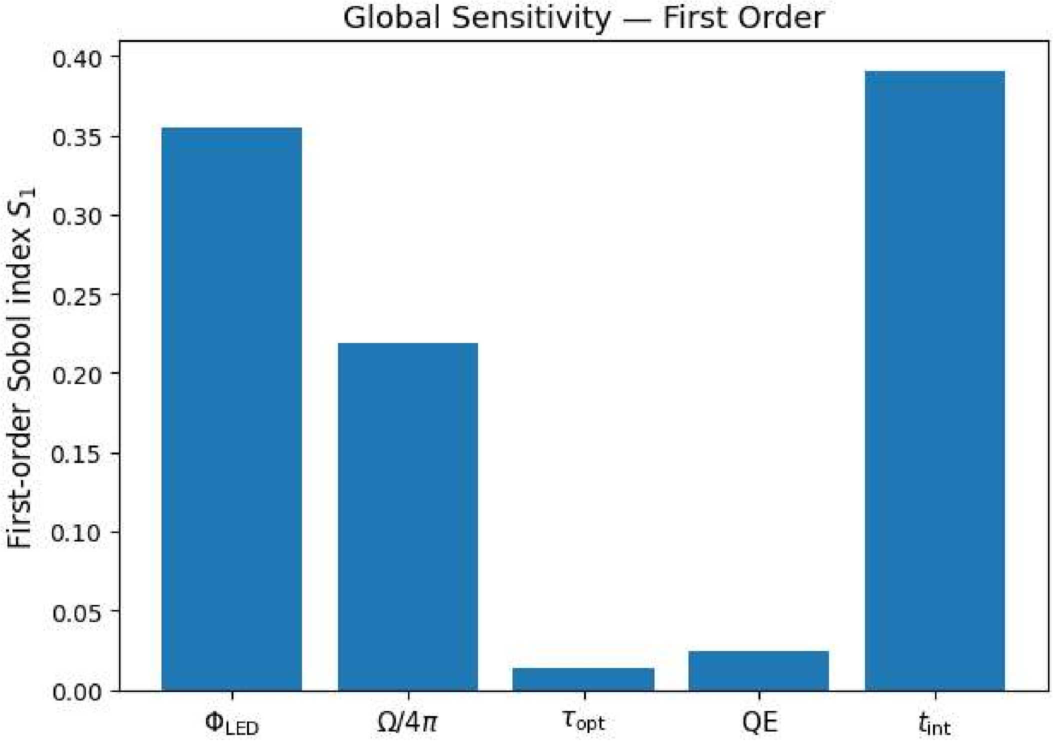

Figure 4-1: First-order Sobol indices (S_1) for the photon-budget model expressed in $\log_{10} LOD(ppb)$. The ranking shows that LED radiant flux and integration time dominate

sensitivity, followed by collection solid angle. Optical throughput and detector quantum efficiency contribute marginally. Indices sum to ~1, indicating variance is largely explained by main effects.

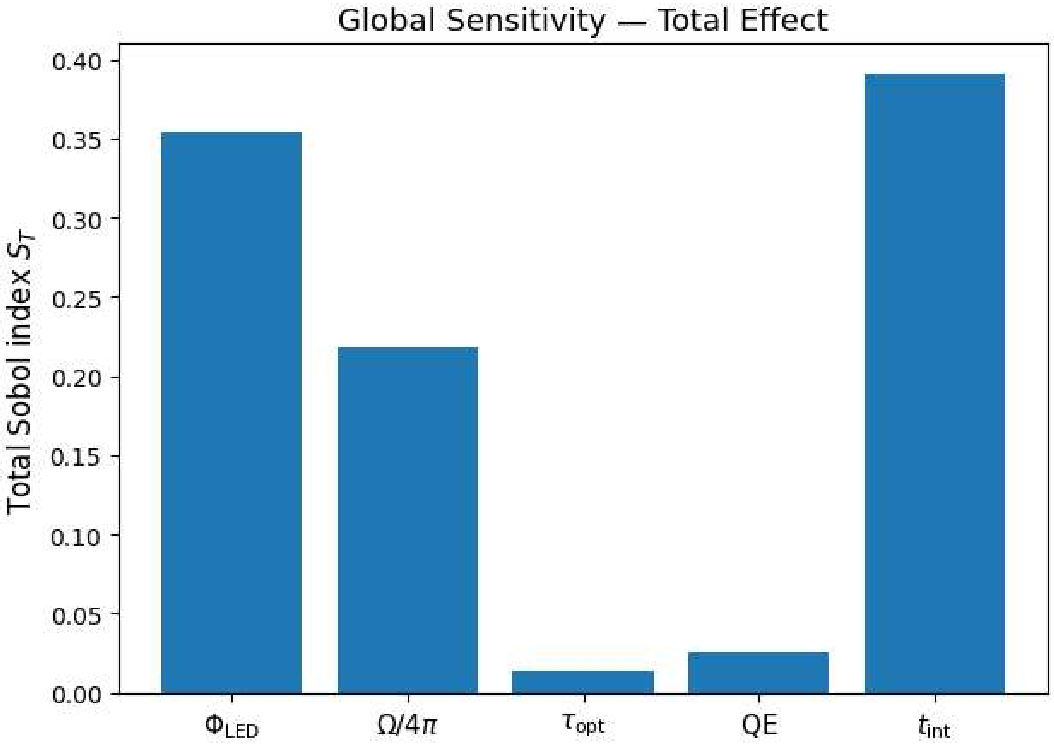

Figure 4-2: Total-effect Sobol indices (S_T) for the same model. Values closely match first-order indices, confirming that parameter interactions are negligible in the shot-noise regime. This validates the use of one-dimensional trade-off analyses (e.g., LED flux vs. solid angle) without needing to account for higher-order couplings.

The Sobol analysis shows a clear ranking of levers. Integration time and LED radiant flux account for the largest share of variance in $\log_{10} LOD$, with collection solid angle as a secondary driver. Optical throughput and detector QE contribute only marginally. First- and total-order indices align closely, indicating negligible interactions and validating one-variable trade-off studies for design decisions.

4.4 TRADE-OFF SURFACES AND ROBUST DESIGN WINDOW

4.4.1 *Optical Power Vs. Collection Solid Angle*

Figure 4-3 shows how LED radiant flux and collection solid angle work together to set the detection limit. Other parameters were held at baseline values. The surface reveals that gains in either parameter improve detection. Higher LED power or larger collection angles both push the limit of detection lower. The diagonal contour pattern suggests the two parameters can partially compensate for each other. But returns diminish beyond about 7-8 mW of LED power or a collection solid angle above 2.5×10^{-3}. The contours become more closely spaced at higher values, meaning each additional increment produces smaller improvements.

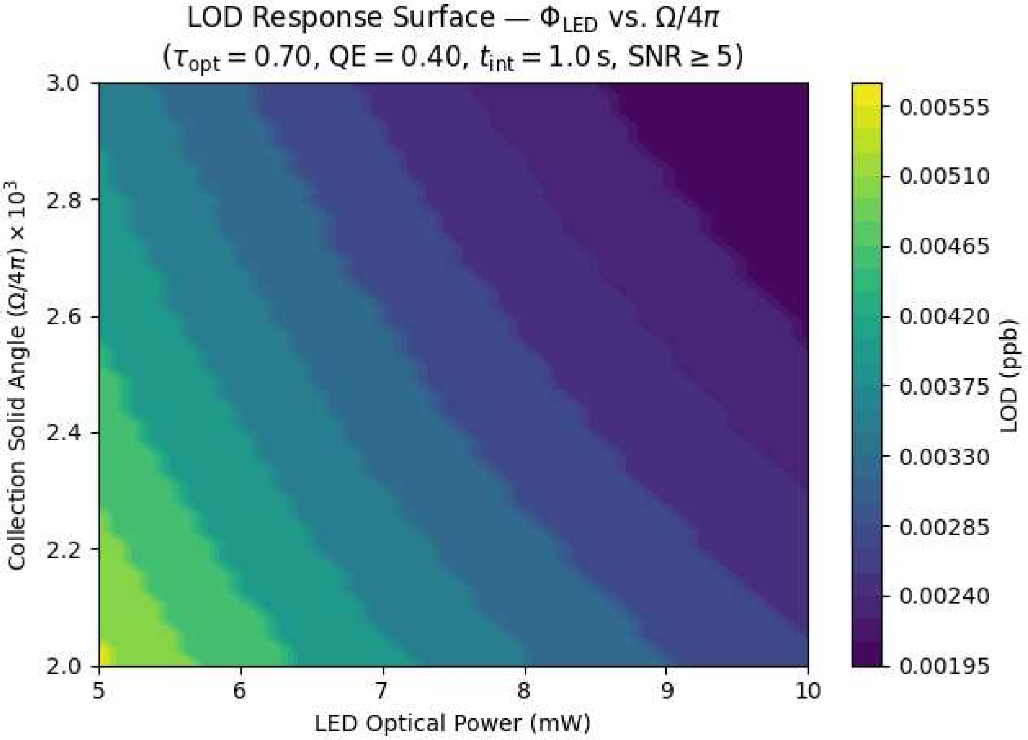

Figure 4-3: Response surface of predicted LOD (ppb) as a function of LED radiant flux Φ_{LED} and collection solid angle $\frac{\Omega}{4\pi}$. Other parameters were fixed at $\tau_{opt} = 0.70$, detector quantum

efficiency $QE = 0.40$, and $t_{int} = 1\ s$. Both levers improve sensitivity, but gains saturate once either LED power exceeds ~8 mW or the collected solid angle exceeds ~2.5 × 10^{-3}. This illustrates the diminishing-returns regime predicted by the global sensitivity analysis and shows that modest increases in both parameters are more effective than overdriving one alone.

The diagonal contours reveal something useful. LED power and collection angle can substitute for each other to some degree. A weak LED can be offset by collecting more light, and the opposite works too. Both parameters start giving diminishing returns around 8 mW for the LED and 2.5 × 10^{-3} for collection angle. Push past these points and the contours flatten out. What does this mean for design? Balancing both parameters works better than maxing out one while ignoring the other. Consider a 10 mW LED with poor light collection. It actually performs worse than moderate settings for both.

4.4.2 *LED Power Vs Lens Diameter*

Collection efficiency starts as fractional solid angle (Ω/4π), which comes straight from the radiometric model. This keeps the analysis general without tying it to specific optics. The problem is that solid angle feels abstract. Outside radiometry, it rarely shows up in optical specs. Figure 4-4 recasts everything in terms of lens diameter instead. A fixed working distance converts geometry into solid-angle capture. Lens diameter makes practical sense for instrument design since that's how portable optics get specified. The examples here use simple singlet lenses. But the approach works just as well for compound lenses, aspheres, and fiber couplers. Effective collection area governs performance across all these cases.

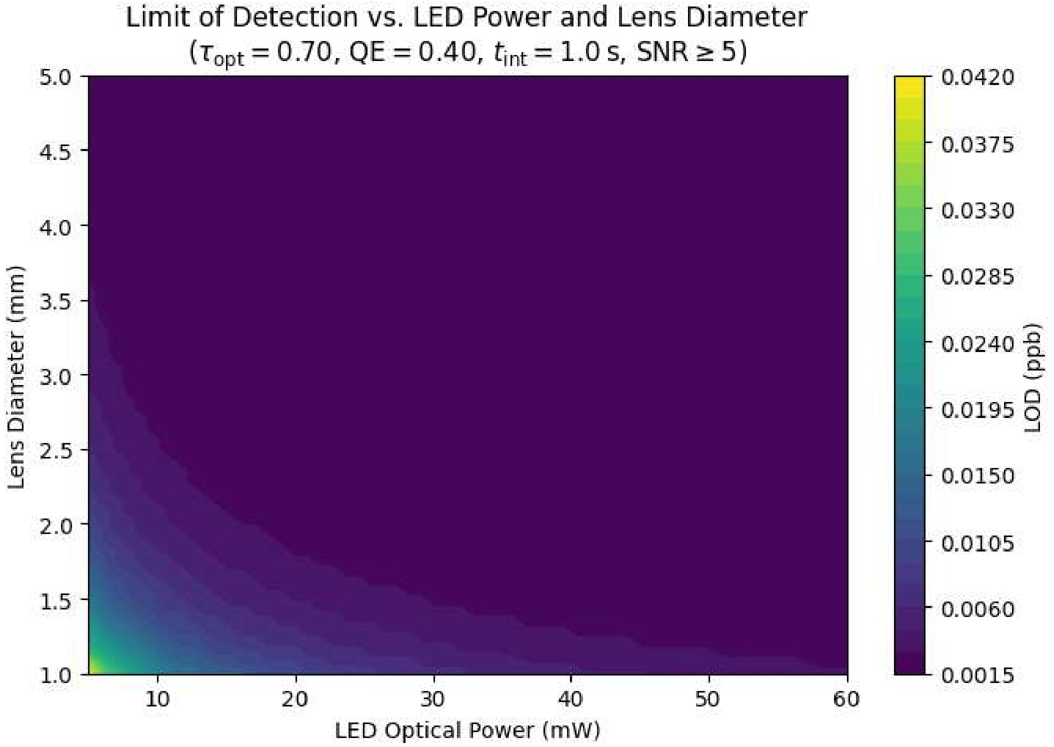

Figure 4-4: Response surface of predicted LOD (ppb) as a function of LED optical power and collection lens diameter. Other parameters were fixed at $\tau_{opt} = 0.70$, detector quantum efficiency $QE = 0.40$, and $t_{int} = 1\ s$. Both levers improve sensitivity, but gains saturate once either LED power exceeds ~8 mW or the collected solid angle exceeds ~2.5×10^{-3}. Lower values correspond to better sensitivity. Both LED power and lens size reduce LOD, but diminishing returns occur above ~30 mW and ~3 mm. This suggests that compact optics combined with moderate LED drive are sufficient to achieve sub-ppb detection under field-relevant conditions.

Figure 4-4 illustrates the combined influence of LED optical power and lens diameter on the achievable limit of detection. Both parameters lower the limit of detection (LOD), though not in equal measure. Their effects are nonlinear. Performance suffers badly at small lens diameters (below 2 mm) or low LED powers (below 10 mW). The LOD gradients get steep in these regions. As either variable increases, the LOD improves rapidly at first. Then it plateaus. Further gains become marginal past this point. This pattern ended up guiding the hardware selection process.

System sensitivity gets bottlenecked by whichever parameter happens to be weaker. Insufficient excitation flux cannot be compensated for by larger optics, no matter how well designed. A powerful LED paired with a small aperture similarly wastes most of its output. The design strategy adopted here prioritizes balance over brute force. Moderate increases in both power and collection area consistently outperform pushing one parameter to extremes while neglecting the other.

4.4.3 *Optical Throughput Limits*

Figure 4-5 maps the combined contribution of filter transmission (τ_filter) and detector quantum efficiency (QE) to the effective opto-electronic throughput of the system. Both factors act multiplicatively. Their product sets an upper bound on the fraction of emitted photons that are ultimately registered as signal electrons. The contour map shows the smooth, monotonic increase in throughput with either improved filter transmission or higher detector QE. This relationship ended up underscoring the importance of optimizing both components simultaneously. A highly efficient detector cannot compensate for a lossy filter. Conversely, even near-unity filter transmission delivers limited benefit if QE remains low.

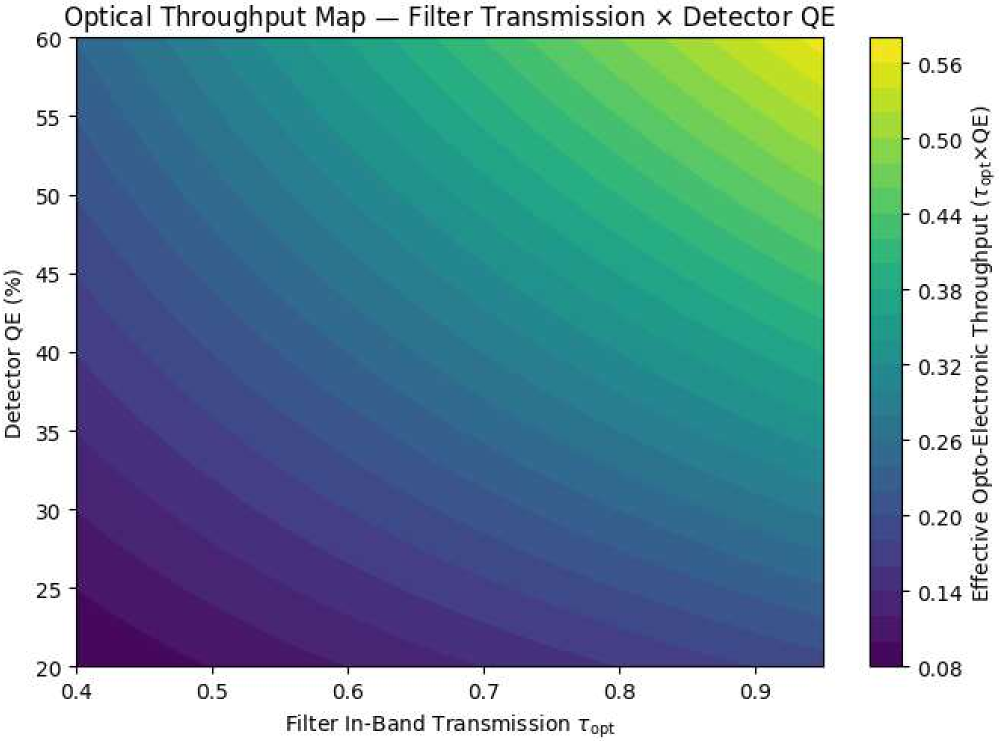

Figure 4-5: Response surface of predicted LOD (ppb) as a function of LED optical power and collection lens diameter. Other parameters were fixed at $\tau_{opt} = 0.70$, detector quantum efficiency $QE = 0.40$, and $t_{int} = 1\ s$. Both levers improve sensitivity, but gains saturate once either LED power exceeds ~8 mW or the collected solid angle exceeds ~2.5 × 10^{-3}. Lower values correspond to better sensitivity. Both LED power and lens size reduce LOD, but diminishing returns occur above ~30 mW and ~3 mm. This suggests that compact optics combined with moderate LED drive are sufficient to achieve sub-ppb detection under field-relevant conditions.

In practical terms, the commercially available ranges restrict achievable throughput to roughly 0.1–0.5. Interference filters run from 50–90% transmission, and compact CMOS detectors offer 25–55% quantum efficiency. This ceiling ended up defining a hard constraint on instrument sensitivity. Photon throughput feeds directly into the shot-noise limit. Incremental gains in either τ_{filter} or QE yield disproportionately large improvements in detection capability at the lower end of their ranges. Diminishing returns show up as both parameters approach their practical maxima.

The map ended up clarifying that improvements in filter coatings and detector architecture remain as impactful as increased excitation power. This holds particularly for low-signal applications where every detected photon carries weight.

4.5 POWER USAGE VS BATTERY LIFE

Figure 4-6 evaluates how integration time and optical power draw jointly determine battery life for a portable fluorescence instrument. The trends ended up showing two competing influences. Longer integration times appear to extend duty cycle efficiency. Overhead operations such as detector readout and LED switching take up a smaller fraction of each acquisition. This effect seems to improve runtime most strongly at sub-second exposures. At those short durations, overhead becomes comparable to active integration. Beyond roughly 2–3 seconds, the benefit tapers off. Pushing t_{int} further offers little additional extension past that point.

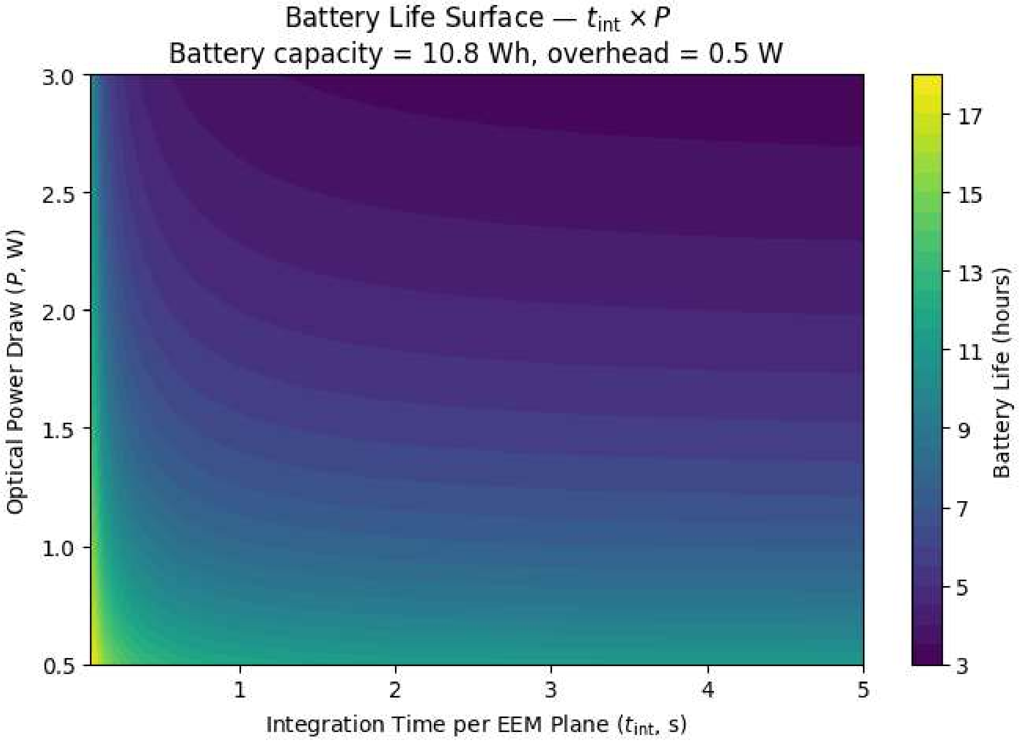

Figure 4-6: Battery life surface as a function of integration time per EEM plane (t_{int}) and optical power draw (P). The map assumes a 10.8 Wh battery pack with 0.5 W overhead for control electronics. Longer integration times reduce duty cycle and extend runtime at fixed optical draw, while higher optical loads shorten runtime. The contour plot highlights the trade-off between sensitivity (favoring longer t_{int} and higher PPP) and field portability (favoring lower average consumption).

Higher optical loads feed directly into higher average power draw. Runtime drops in a near-linear fashion as a result. At the upper end of the modeled range (roughly 3 W), runtime falls to just a few hours. Moderate loads (roughly 1 W) let the system run for well over 10 hours. These results ended up framing what appears to be an essential trade-off for field deployment. Pushing sensitivity higher through stronger excitation and longer integrations seems to improve detection but eats into runtime at the same time. Prioritizing endurance probably means holding back on both parameters.

In practice, this balance ends up depending on the survey protocol at hand. Short screening campaigns can tolerate high power settings. Detection limits get pushed lower as a result. All-day monitoring efforts seem to need conservative settings to keep things running uninterrupted. Integration time works best as a tuning factor at short exposures, as the surface map clarified. Reducing optical load appears to be the go-to for extending battery life across all regimes.

4.6 CONSTRAINT: MATRIX EFFECTS AND ENVIRONMENTAL ATTENUATION

Although the model in Chapter 3 assumes pristine optical conditions, environmental factors such as turbidity, re-absorption, and scattering can possibly reduce the number of fluorescence photons that reach the detector. These losses are summarized by a matrix factor M in the range

$0 < M \leq 1$. Where values near 1 correspond to clear laboratory water and values closer to 0.5 approximate turbid surface runoff or raw process samples.

The matrix factor enters the photon budget with the optical collection terms:

$$\dot{N}_{coll} = \dot{N}_{emit} \times \frac{\Omega}{4\pi} \times \tau_{opt} \times M \tag{4-1}$$

which lowers the detected photon rate without altering the scaling of design-controlled parameters. In the shot-noise limit, this yields

$$SNR \propto \sqrt{M}, \qquad LOD \propto M^{-\frac{1}{2}} \tag{4-2}$$

As a result, halving M from 1.0 to 0.5 reduces SNR by ~29% and increases the limit of detection by ~41%. While M is not a hardware lever, it is included here as a constraint on field performance.

4.7 UNCERTAINTY PROPAGATION AND SCENARIO TESTING

The Monte Carlo histogram in Figure 4-7 illustrates how variability in LED power, optics, and detector performance spreads achievable detection limits across a wide range. Even within realistic design bounds, the resulting LODs span nearly two orders of magnitude. This shows that sensitivity is best understood as a distribution rather than a single value.

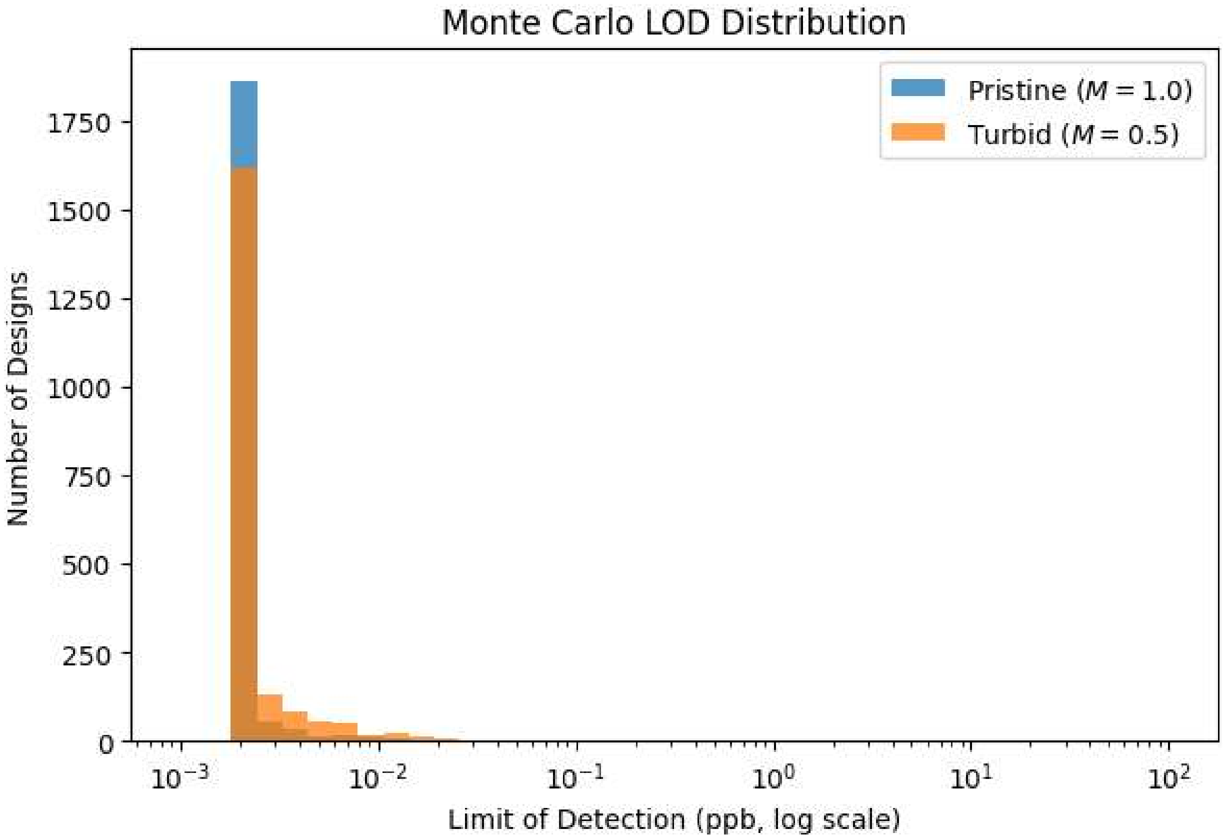

Figure 4-7: Monte Carlo distributions of predicted limits of detection (LOD) across 1,000 randomized instrument designs. Each design varies LED power, collection solid angle, optical transmission, detector quantum efficiency, and integration time within practical ranges. Results are shown for pristine water ($M = 1.0$) and turbid runoff ($M = 0.5$). Left: histograms of LOD values on a logarithmic x-axis highlight the shift toward higher detection limits in turbid conditions. Right: pass fraction under a 10 ppb performance criterion, showing reduced success rate when scattering and self-absorption degrade optical throughput.

From the comparison above between pristine (M = 1.0) and turbid (M = 0.5) conditions, there is a shift toward higher detection limits. Scattering and self-absorption drive this change. The histogram ended up revealing how large this effect gets. Clear water designs cluster tightly in the low-ppb regime, with the peak sitting around 0.002 to 0.003 ppb. Turbid conditions broaden the distribution. This lines up with the theoretical penalty from halving photon collection. Overlap between the two distributions appears minimal. Environmental effects seem to act as a systematic penalty on performance as a result. Hardware performance drops even when it stays unchanged.

The spread within each condition stands out as particularly notable. Pristine conditions still show achievable LODs ranging from roughly 0.001 to 0.01 ppb. This is a full order of magnitude difference from solely hardware variability. The turbid distribution shows similar relative spread but at higher absolute values. These results also suggest that hardware design and environmental effects need to be considered together. Laboratory-measured sensitivity in ideal conditions does not capture what happens in the field. For a robust design, this means acceptable detection limits must hold up across the entire distribution. The best-case values do not represent what typically occurs in practice.

Chapter 5. EXPERIEMENTAL RESULTS

5.1 CHAPTER OVERVIEW

The theoretical analysis and sensitivity modeling from previous chapters established the possible detection limits, optical tradeoffs, and parameter sensitivities for a portable EEM device. Testing whether those predictions actually hold under experimental conditions ended up being the next step. This chapter presents proof-of-concept measurements exploring what a portable system might achieve in practice. The goal was straightforward: see if the modeled performance translates to detectable pesticide signatures in simple aqueous solutions. Feasibility mattered more than optimization at this stage. Getting the system working seemed more important initially.

These experiments had three objectives. First, establish baseline fluorescence of deionized water and quantify system artifacts needing attention. Background signal needed understanding before attempting low-level contaminant detection. Without knowing what the instrument sees in pure water, pesticide signals become hard to interpret. Second, generate excitation–emission matrices for representative pesticides. The dilution series spanned 1000 ppb down to 0.1 ppb. This range was chosen to bracket expected detection limits and meet field monitoring requirements. Third, compare observed signal strength with radiometric model predictions. These comparisons ended up assessing practical detection limits and revealing variability across compound classes.

Three pesticides were chosen: zeta-cypermethrin, glyphosate, and myclobutanil. The selection was based on available pesticides and photophysics reviewed earlier in Section 2.1. These compounds span different quantum yield ranges. Testing this range seemed necessary to see if Chapter 4 detection limits hold across different compound classes. All measurements in the following chapter used serial dilutions of commercially available concentrations in deionized water. Matrix effects get isolated this way by focusing on intrinsic fluorescence. Clean solutions provided the starting point to establish baseline performance before real water complications can be studied.

The experimental work proceeded through several stages. Documenting the experimental setup came first. Whether results mean anything depends on getting instrumentation, sample preparation, and data acquisition right. Baseline characterization of deionized water came next. Background signal sets the noise floor for detection of pesticides, so understanding what the instrument sees in pure water is essential. Each pesticide was then measured across a dilution series spanning 1000 ppb down to 0.1 ppb. This range brackets what the radiometric model predicted.

Detection thresholds and spectral features get compared across the three compounds to assess whether chemical structure affects performance as expected.

5.2 MATERIALS AND METHODS

5.2.1 *Instrumentation*

The experimental setup consisted of a UV LED driver, excitation LED, optical fiber coupling, quartz cuvette holder, and an Ocean Optics Flame spectrometer arranged as shown in Figure 5-1. This configuration enabled controlled excitation of aqueous pesticide samples and collection of emission spectra across the UV–visible range while down sampling can be used for future results.

All fluorescence measurements used an Ocean Optics Flame miniature spectrometer covering 200–800 nm. The system was configured for fluorescent excitation–emission scans. Excitation came from narrowband UV–visible LEDs spanning 200–400 nm, coupled into a standard 1 cm quartz cuvette. The emission power for each LED 1.6 mW at 290nm, 0.33 mW at 341nm 1 mW at 366nm, 6 mW at 405nm, and 8 mW 430nm. There were attempts to purchase higher intensity LEDs, however, this was not feasible in the timeframe. The spectrometer operated with fixed CCD gain. Integration time was set to 60 seconds per excitation wavelength. While signals were detectable at 1-second integration (as modeled in Chapter 4), they were extremely weak at low concentrations. The longer integration time was needed to collect sufficient photons. This likely reflects both the photon distribution across the emission spectrum and differences in spectrometer sensitivity between the modeled Hamamatsu spectometers and the Ocean Optics Flame used here. Further work is required to reduce integration time for practical field deployment. Instrument stability needed monitoring throughout each measurement sequence. Blanks got re-run every four samples. Any blank exceeding three times the baseline standard deviation triggered a rerun of the preceding sequence.

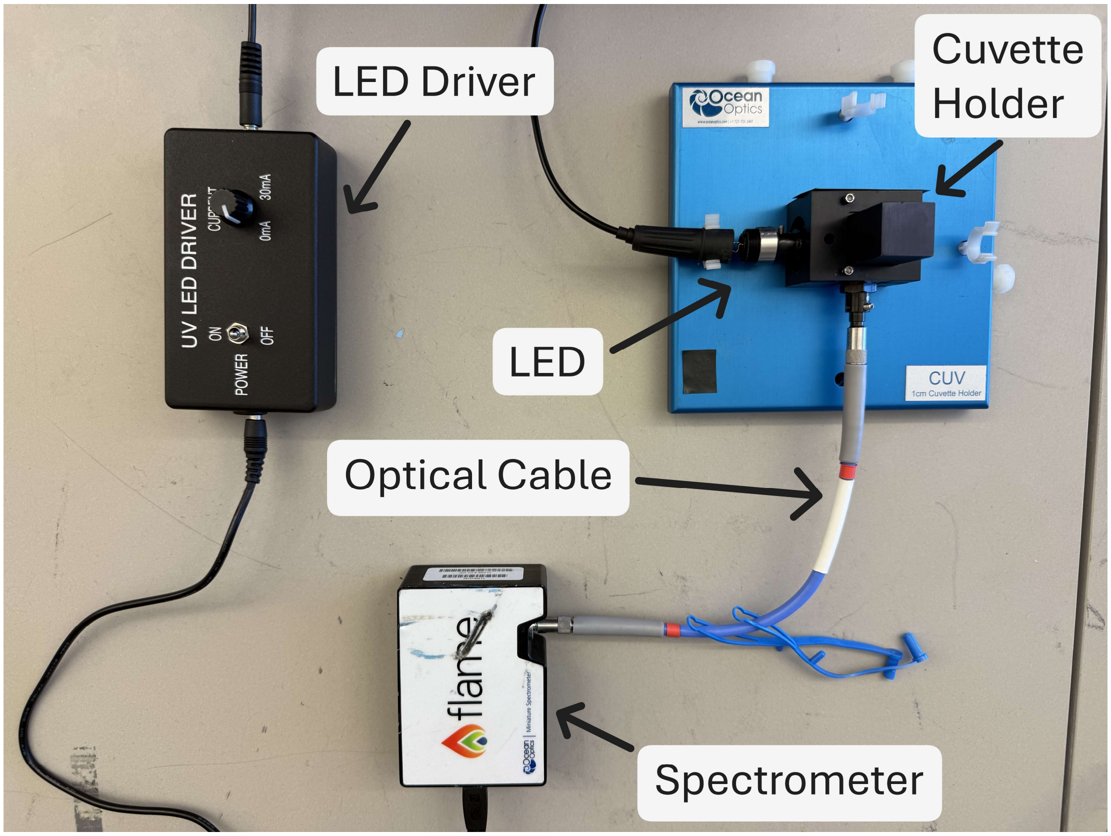

Figure 5-1 Experimental testbench for EEM fluorescence measurements. The system includes a UV LED driver, excitation LED source, optical fiber coupling, a 1 cm quartz cuvette holder, and an Ocean Optics Flame miniature spectrometer. The setup allows excitation of aqueous samples with UV–visible light and collection of fluorescence spectra for subsequent processing.

5.2.2 *Sample Preparation*

Stock solutions of the three pesticides were prepared from manufacturer-supplied materials and serially diluted in deionized (DI) water to yield nominal concentrations of 1000, 100, 10, 1, and 0.1 ppb. All glassware was rinsed and dried between samples to prevent cross-contamination. DI water served both as the blank reference and as the solvent for all dilutions.

5.2.3 *Data Acquisition*

For each sample, an excitation–emission matrix was collected by changing out the excitation LED source across the available UV–visible range and recording the corresponding emission spectra. The raw data were stored as two-dimensional slices with each corresponding to a single excitation wavelength. EEM cubes were reconstructed by concatenating slices and aligned on a common emission axis. To minimize instrument artifacts, the DI water baseline was subtracted from each sample scan. In addition, per-excitation normalization was applied to account for LED power fluctuations and spectrometer sensitivity drift.

5.2.4 *Controls and Quality Assurance*

Blank DI water scans are the baseline spectral features of the system. These control samples were run at each concentration level before sampling. This done to remove reflected and scattered noise from the pesticide samples. This also verified that observed pesticide signals exceeded background variation. Signal stability was also needed for each round of sampling. LED output and detector response could drift over the multi-hour measurement sequences. All pesticide EEMs were visually inspected for concentration-dependent structure. This confirmed that detected features came from the analyte rather than systematic noise. Separating signals from artifacts mattered most at the lowest concentrations when signal-to-noise ratios approached the detection threshold.

5.2.5 *Measurement Protocol and Limitations*

All measurements represent single acquisitions per concentration level. Replicate measurements, formal error propagation, and statistical validation of detection limits were deferred to future work. The focus of this experimental chapter is demonstrating proof-of-concept detectability and validating the radiometric model's qualitative predictions (compound ranking) rather than establishing rigorously validated analytical methods. The benchtop system serves as a controlled testbed for model validation, not as a finalized analytical instrument.

5.3 BASELINE RESULTS WITH DEIONIZED WATER

Deionized water scans established the system background across the same excitation range used for pesticide samples. Figure 5-2 shows representative EEMs for DI water at each nominal concentration level (1000, 100, 10, 1, and 0.1 ppb). Consistent features appeared across all concentration levels. The most prominent was a bright emission band between 400-450 nm when excited at 405-430 nm. A second, weaker feature appeared around 350-380 nm emission with excitation at 341-366 nm. The primary band came from Raman scattering of water. The secondary feature likely came from trace impurities in the cuvette or optical path.

Band intensities stayed stable across repeated scans and concentration levels. This confirmed the features came from the instrument-matrix system rather than sample contamination. The consistency across nominal concentration levels (which contained no pesticide) further verified these were background artifacts. The DI water spectra provided a reference for baseline subtraction. The baseline was subtracted slice by slice from each excitation step. This ensured emission features from pesticides exceeded the noise floor established by the blank.

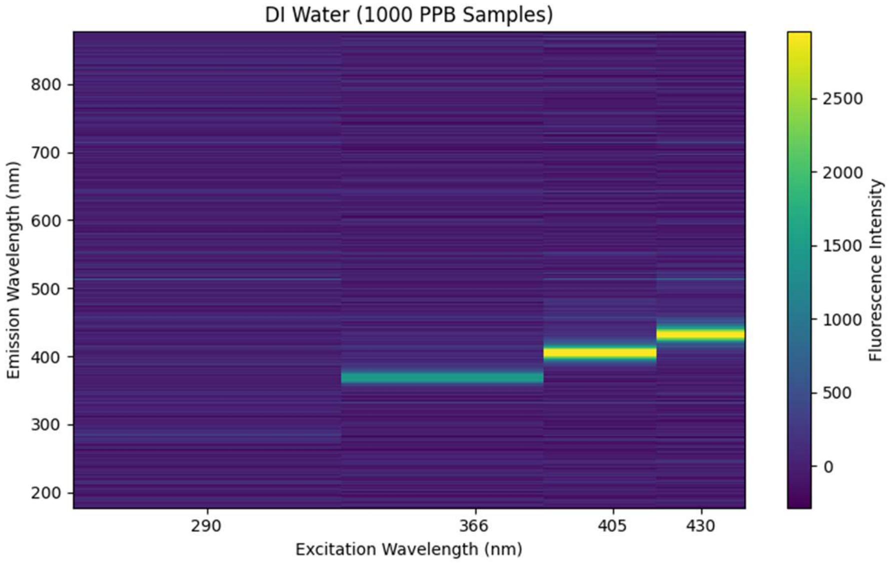

Figure 5-2a. DI water baseline for 1000 PPB samples.

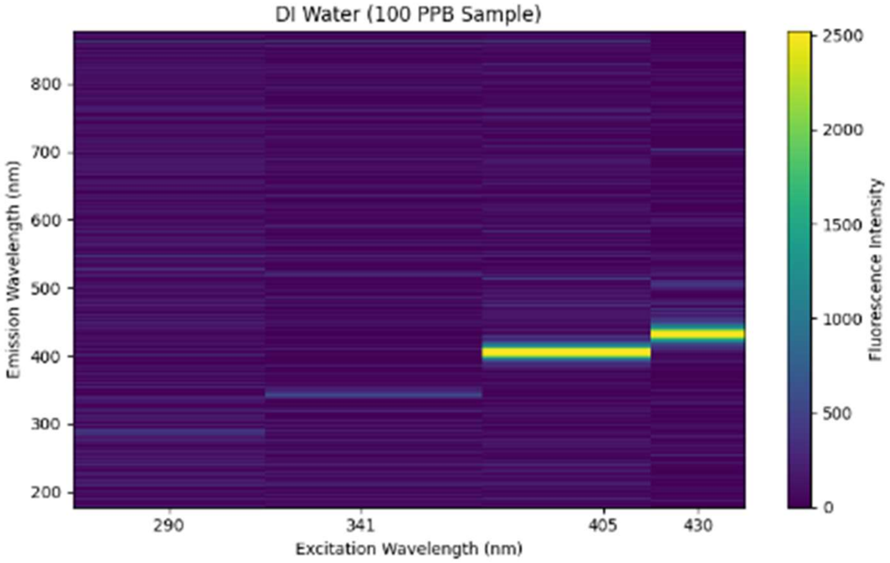

Figure 5-2b. DI water baseline for 100 PPB samples.

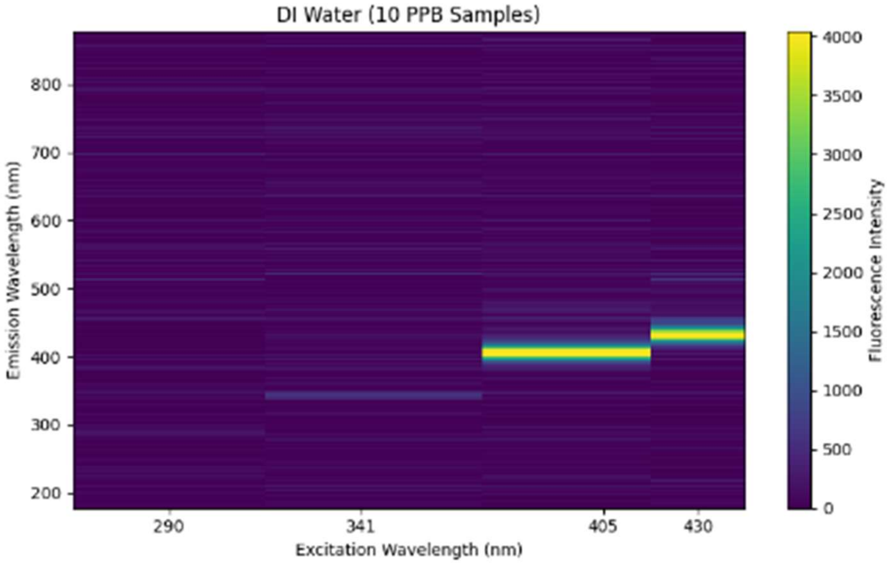

Figure 5-2c. DI water baseline for 10 PPB samples.

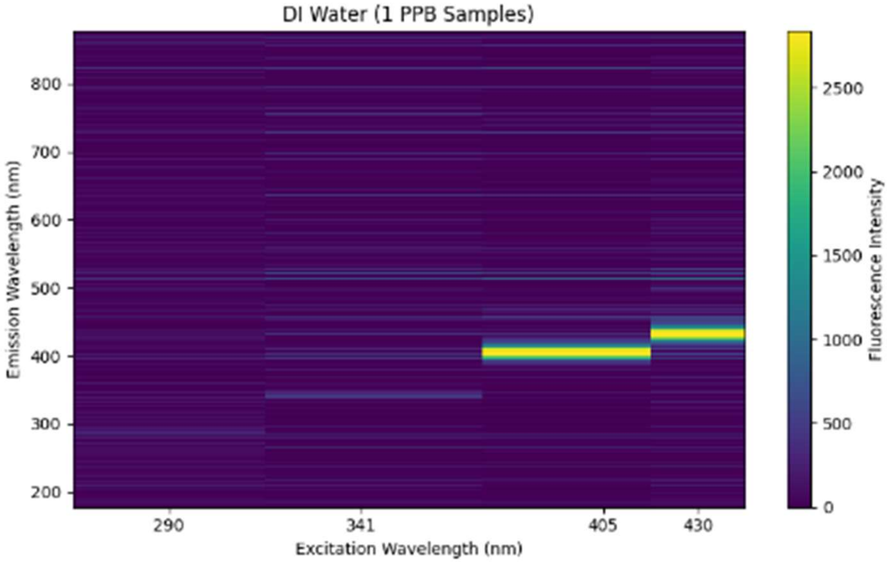

Figure 5-2d. DI water baseline for 1 PPB samples.

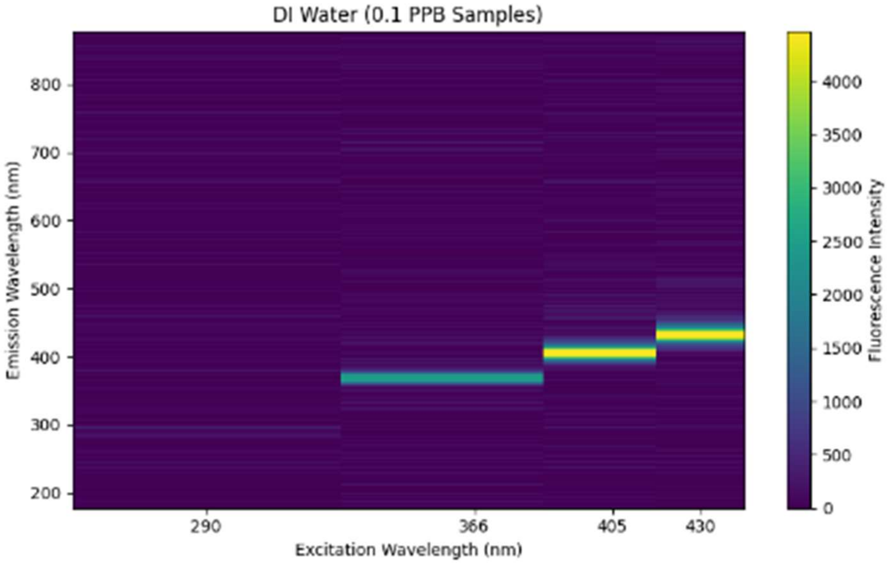

Figure 5-2e. DI water baseline for 0.1 PPB samples.

Figure 5-2 Excitation–emission scans of deionized (DI) water collected at nominal pesticide dilution levels (1000, 100, 10, 1, and 0.1 ppb). All spectra show a consistent emission feature between 350–500 nm, attributed to Raman scattering of water and minor optical-path artifacts. The stability of this feature across runs confirms its suitability for baseline subtraction in subsequent pesticide measurements.

5.4 ZETA-CYPERMETHRIN RESULTS

Concentration-dependent fluorescence features showed up in the zeta-cypermethrin scans. Higher concentrations were clearly detectable. Trace levels were close to the noise floor. Figure 5-3 shows the normalized EEM cubes across the dilution series from 1000 ppb down to 0.1 ppb.

At 1000 ppb and 100 ppb, emission bands centered around 400-450 nm appeared strong when excited at 405-430 nm. These features stood out clearly above baseline water fluorescence. The sharp contours at 1000 ppb confirmed robust emission from the structure under UV–visible excitation. At 100 ppb, the same emission pattern showed up with reduced magnitude. After per-slice normalization, spectral shape stayed consistent. This consistency across the two highest concentrations ended up validating the emission fingerprint for zeta-cypermethrin.

Signal quality took a sharp turn at 10 ppb. A faint emission feature hung on near 405 nm excitation. Horizontal noise artifacts crept across the emission axis at the same time. The structured band became nearly impossible to separate from background. The signal was closing in on the detector's noise floor. Weak emission remained near the 405-430 nm excitation region at 1 ppb. Signal-to-noise continued its downward slide. Identifying the compound with confidence required comparing across the concentration series.

At 0.1 ppb, structured emission gave way to noise. Horizontal banding artifacts took over the EEM. Near 290 nm excitation, there is a possible weak feature at 330 nm, however, more tests are needed. Separating it from instrument noise proved unreliable at this concentration. Between 10 ppb and 100 ppb appears to be the practical detection limit for zeta-cypermethrin under these experimental conditions.

The detection range fell well short of the sub-ppb limits Chapter 4 predicted. What went wrong? Several factors came into play. The 60-second integration time collected more photons than the modeled 1 second, but still could not make up for system losses elsewhere. The Ocean Optics Flame spectrometer brought a higher noise floor than the modeled spectrometer. LED output and collection efficiency in the actual benchtop setup did not match the idealized assumptions. Photon throughput took a hit. Even in deionized water, matrix effects may have chipped away at signal strength beyond what baseline corrections could fix.

Still, the results show zeta-cypermethrin can be tracked at concentrations that matter for regulators. The system missed the modeled sub-ppb targets, but EPA aquatic-life benchmarks for pyrethroids sit between 0.5 and 10 ppb depending on the compound. The 10-100 ppb range demonstrated here gets within one order of magnitude from regulatory targets. Getting down to sub-ppb sensitivity for field work would take more. LED power needs a boost. Collection optics need refinement. Detector integration needs improvement.

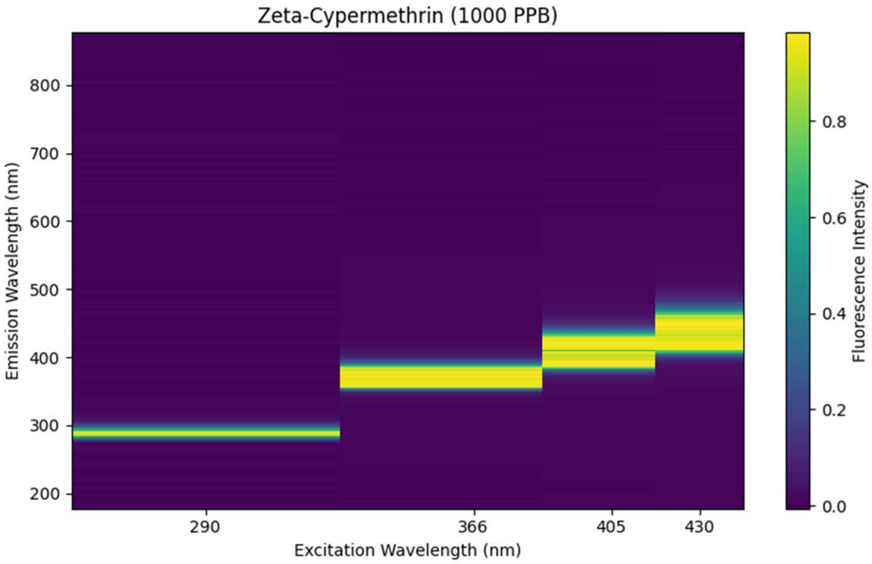

Figure 5-3a. Zeta Cyphermethrin 1000 PPB sample.

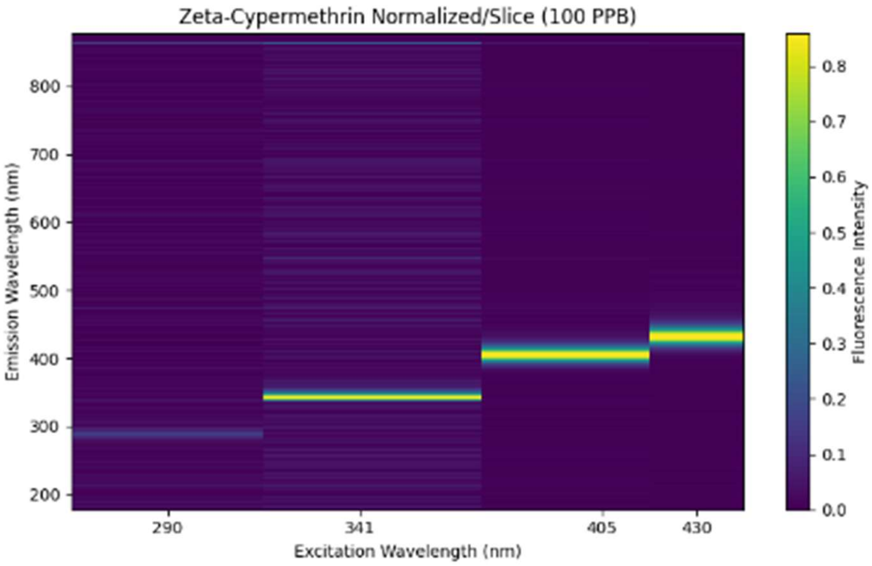

Figure 5-3b. Zeta Cyphermethrin 100 PPB sample.

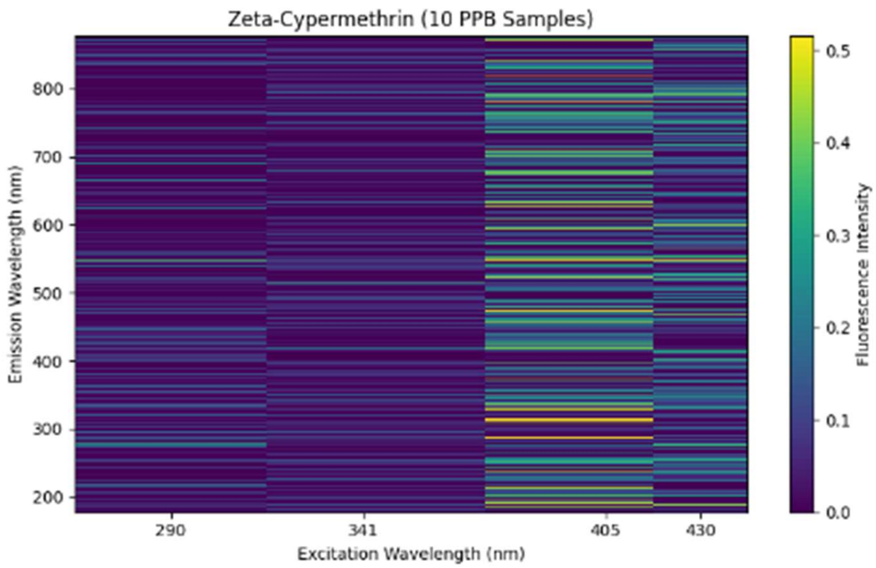

Figure 5-3c. Zeta Cyphermethrin 10 PPB sample.

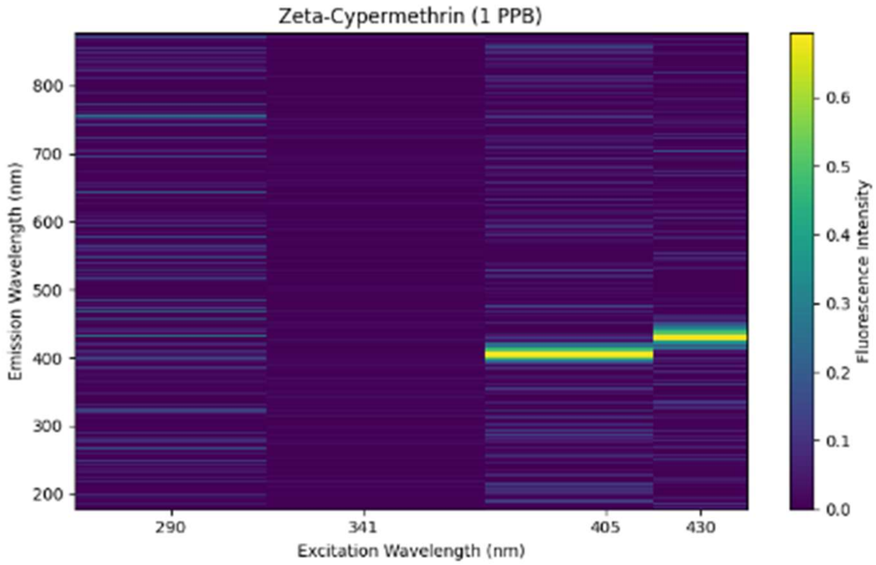

Figure 5-3d. Zeta Cyphermethrin 1.0 PPB sample.

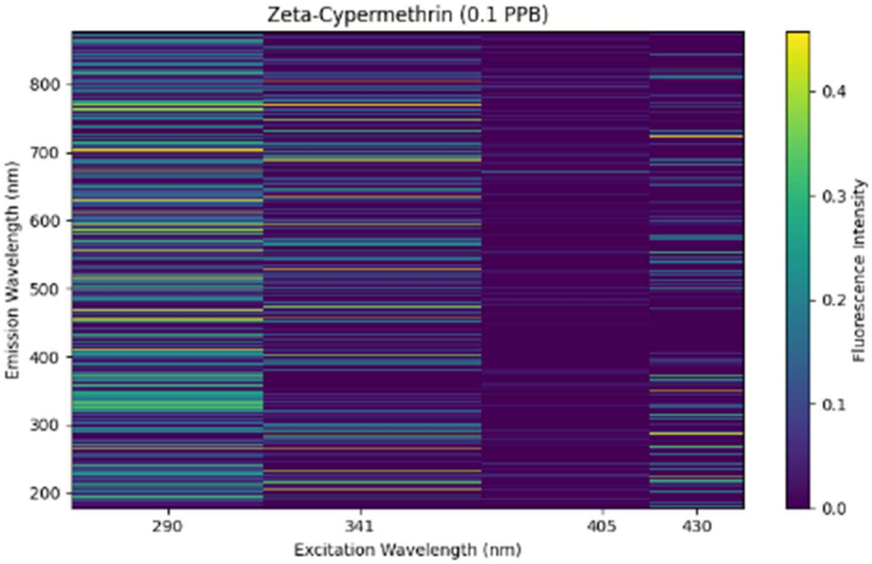

Figure 5-3e. Zeta Cyphermethrin 0.1 PPB sample.

Figure 5-3 Excitation–emission spectra of zeta-cypermethrin across 1000, 100, 10, 1, and 0.1 ppb concentrations. All scans show characteristic fluorescence features between 405–430 nm excitation and 400–450 nm emission, with band intensity decreasing at lower concentrations. Detection appears feasible in the 10-100 ppb range under these experimental conditions.

5.5 GLYPHOSATE RESULTS

Glyphosate showed no detectable fluorescence distinct from baseline across all of the concentration. Figure 5-4 shows the EEM cubes from 1000 ppb down to 0.1 ppb. At all level, no glyphosate-specific emission ridges appeared in the raw excitation–emission matrices. Features visible in these scans matched what DI water blanks showed or were slightly shifted. The bands were around 400-450 nm and had horizontal noise artifacts from normalization.

At 1000 and 100 ppb, the spectra had the same broad emission patterns seen in deionized water controls. Baseline subtraction likely removed some cuvette-related artifacts, however, when normalized they are quite similar. Above the noise floor, no glyphosate-specific signal emerged. Features near 280-300 nm excitation and 300-360 nm emission could not be separated reliably from instrumental artifacts. Glyphosate's presence may have shifted the baseline slightly compared to pure DI water. This shift did not produce a distinguishable fluorescence signature. Any effects from the compound are indistinguishable from background variation.

Horizontal banding noise dominated the EEM cubes at 10 ppb and 1 ppb. Any potential glyphosate signal is weaker than detector noise and baseline drift. The 0.1 ppb dataset showed similar noise characteristics. No structured emission from the analyte appeared.

These results confirm the system cannot detect glyphosate by reagent-free fluorescence. The compound's minimal aromatic conjugation results in extremely low quantum yield. Chemical derivatization would be needed to enhance fluorescence. LC-MS/MS offers an alternative route.

This finding ended up establishing an important limitation for the approach. Strongly fluorescent pesticides like zeta-cypermethrin showed up at 10-100 ppb in the measurements. Glyphosate and similar compounds fell below the noise floor even at 1000 ppb. The data shows reagent-free fluorescence works for pyrethroids and similar aromatic compounds. Non-fluorescent analytes like glyphosate needed derivatization or signal enhancement to be detectable.

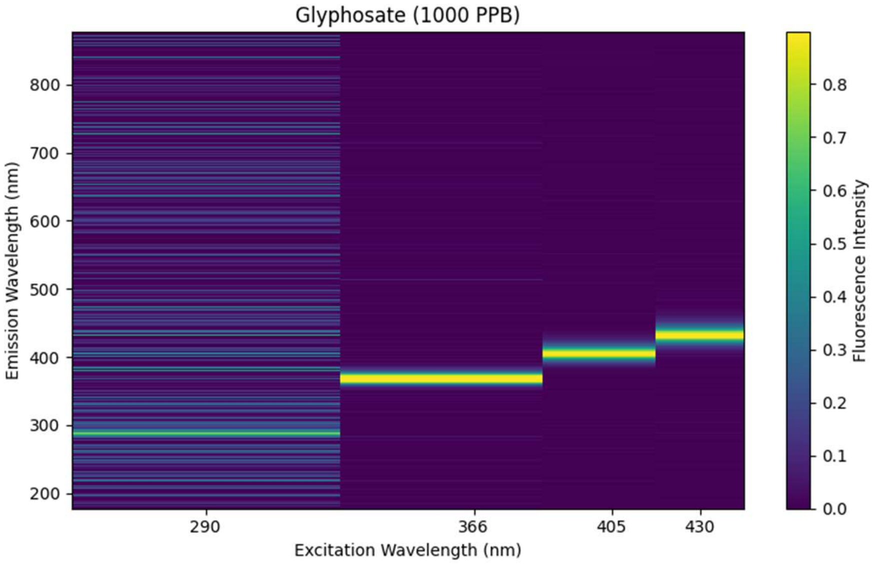

Figure 5-4a. Glyphosate 1000 PPB sample.

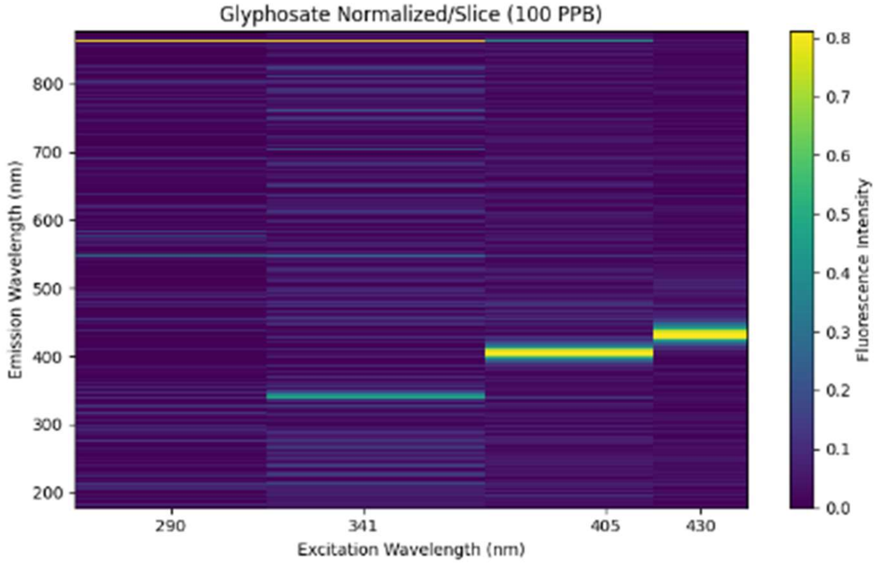

Figure 5-4b. Glyphosate 100 PPB sample.

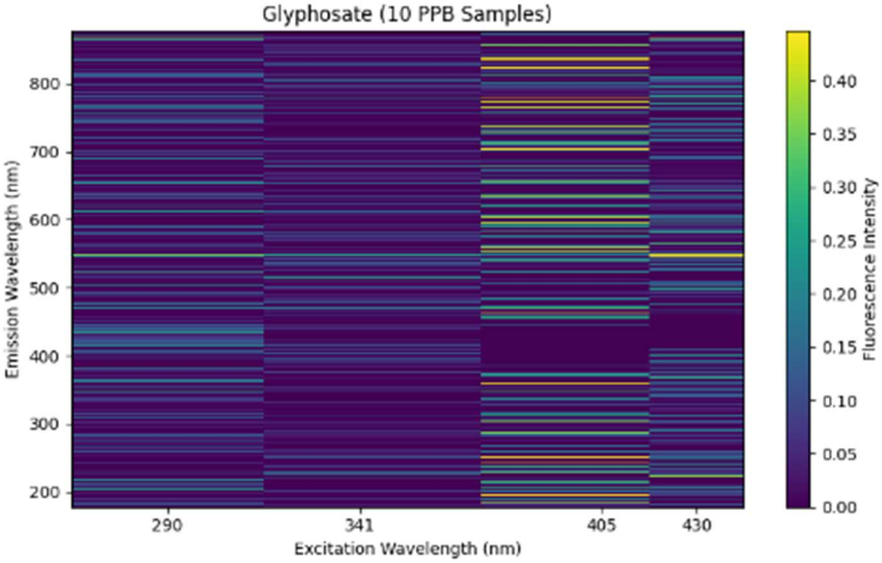

Figure 5-4c. Glyphosate 10 PPB sample.

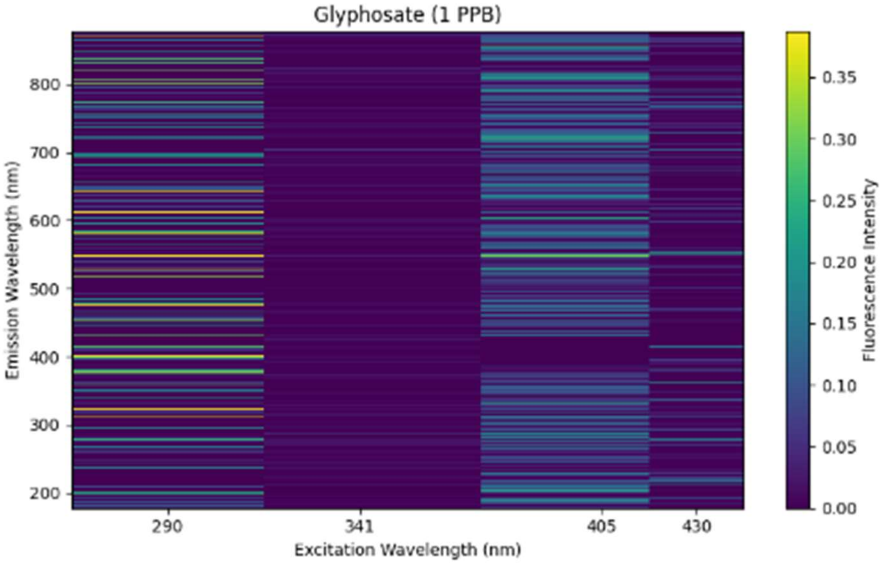

Figure 5-4d. Glyphosate 1.0 PPB sample.

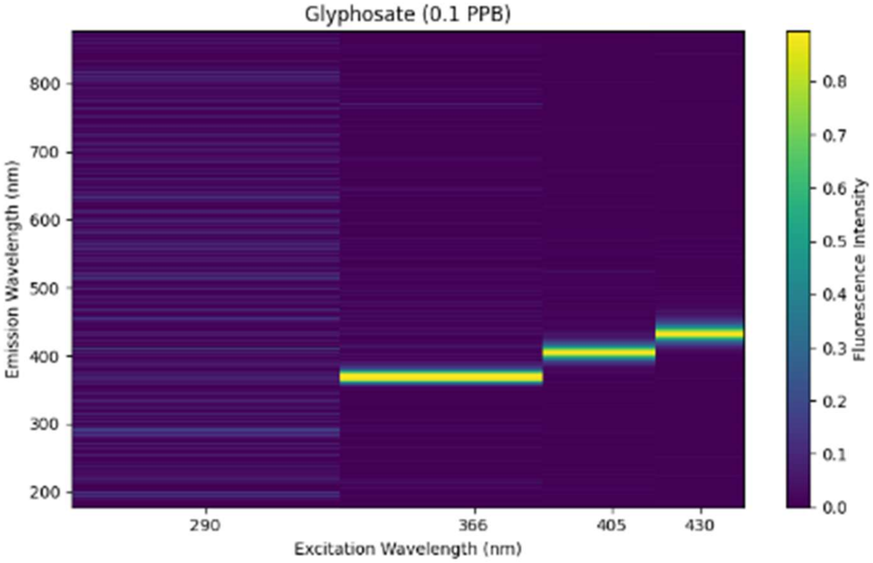

Figure 5-4e. Glyphosate 0.1 PPB sample.

Figure 5-4 Excitation–emission spectra of glyphosate across concentrations from 1000 to 0.1 ppb. No glyphosate-specific fluorescence features could be distinguished from baseline noise and water Raman bands at any concentration level.

5.6 MYCLOBUTANIL RESULTS

Myclobutanil exhibited very detectable fluorescence with a clear emission band under UV excitation at 290 nm excitation. Figure 5-5 shows the normalized EEM cubes from 1000 ppb down to 0.1 ppb. Normalization was used on each to enable cross-concentration comparison and reveal spectral features clearly.

At 1000 and 100 ppb, a distinct emission feature appeared around 280-290 nm excitation and produced emission between 320-360 nm. This band reflects the aromatic character of the triazole fungicide structure. The features visible at 400-450 nm in these scans matched the water Raman bands observed in DI water blanks and should not be attributed to myclobutanil fluorescence.

The UV-excited band remained distinct and reproducible at the two highest concentrations and faded at lower concentrations. Scans at 1000 and 100 ppb showed consistent emission maxima and spectral shape. This result confirmed the features originated from the analyte rather than instrumental drift. Reproducibility matters for building calibration models. The compound's response at these levels suggests myclobutanil could work as a target for chemometric deconvolution in mixed-pesticide samples.

At 10 ppb, signal degradation became noticeable. Horizontal banding noise started to become dominant and spread across the emission axis. At 290 nm excitation, a faint feature remained visible at the 330 nm emission range. Background artifacts obscured it and distinguishing the signal from noise took careful examination. Signal-to-noise dropped at this concentration. This concentration appears to mark a threshold. Below this point, identifying the compound with confidence became more difficult without running multiple replicates or applying chemometric methods.

At 1 ppb and 0.1 ppb, very faint features in the UV excitation region persisted with strong noise interference. Instrumental noise nearly obscured these signals but could possibly be corrected for. Notable is that any structured emission appeared at 0.1 ppb at all. This suggests the UV band might retain trace signatures under optimized conditions. Horizontal banding artifacts dominated both concentration levels. Before claiming detection at these concentrations, additional validation would be needed. Based on these observations, myclobutanil identification appears achievable between 10 ppb and 100 ppb. Reaching below 10 ppb would require optimization work on the UV band.

Getting myclobutanil detection below 10 ppb would require further optimization. At 1 ppb and 0.1 ppb, the faint UV features suggest that Myclobutanil is capable of being detected at these levels. The system's noise floor currently limits how low we can go though. Boosting LED output power between 250 nm and 330 nm could also help push the detection limit down toward 1 ppb. Better collection optics or longer integration time are needed for the final system and will do the same. Chemometric methods like PARAFAC or N-PLS offer another route and augment collection hardware.

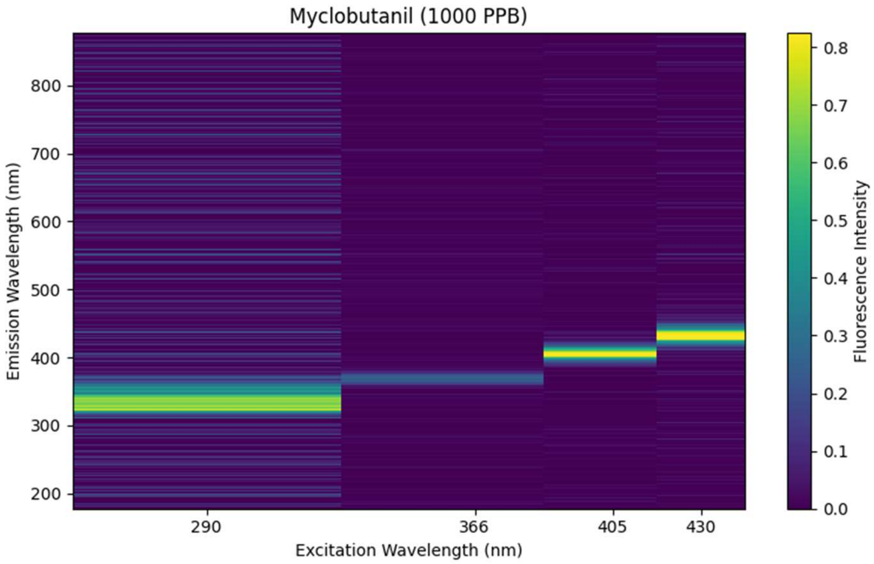

Figure 5-5a. Myclobutanil 1000 PPB sample.

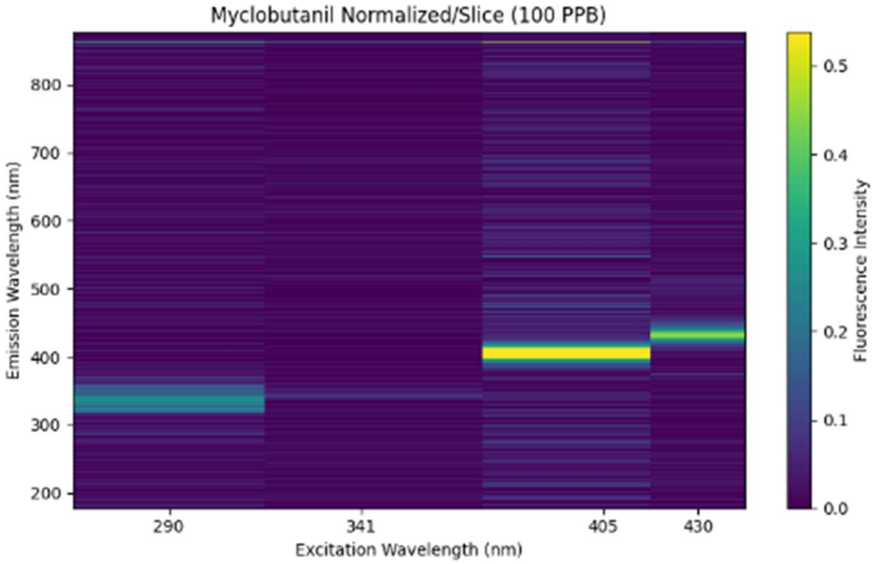

Figure 5-5b. Myclobutanil 100 PPB sample.

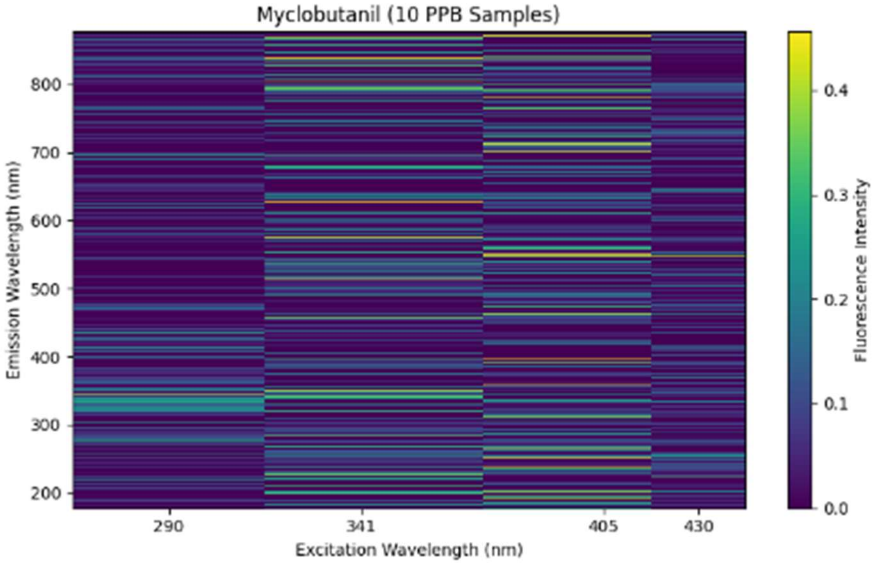

Figure 5-5c. Myclobutanil 10 PPB sample.

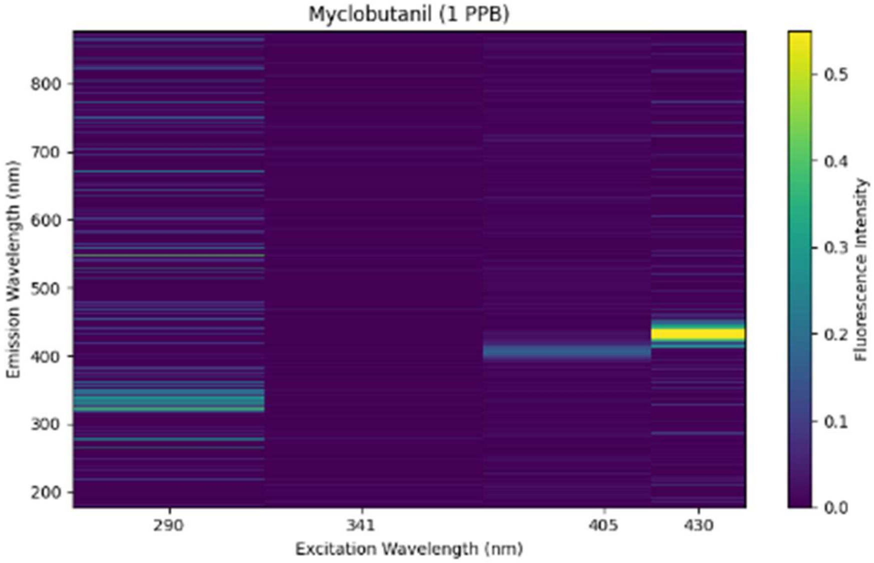

Figure 5-5d. Myclobutanil 0.1 PPB sample.

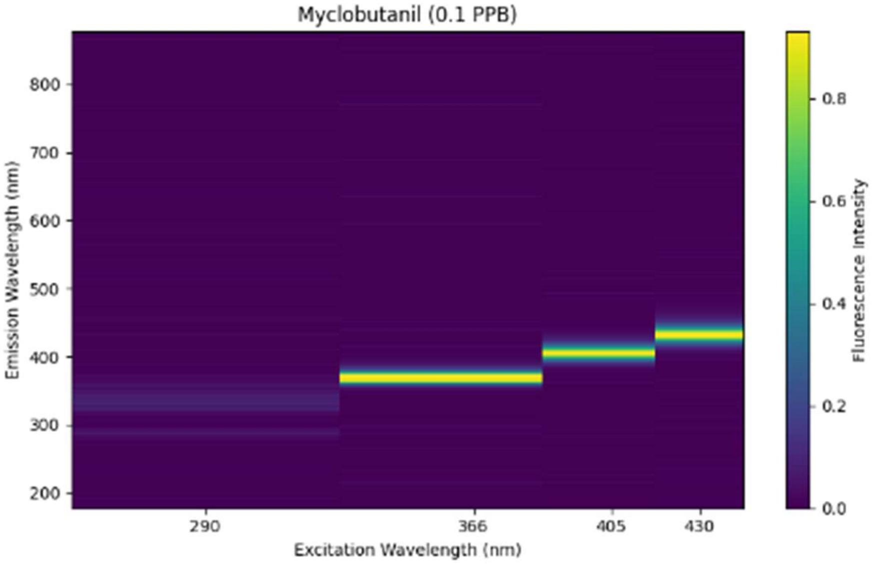

Figure 5-5e. Myclobutanil 0.1 PPB sample.

Figure 5-5: Excitation–emission matrices of myclobutanil across concentrations from 1000 to 0.1 ppb. A characteristic emission band appeared near 320–360 nm under 280–290 nm excitation, reflecting the aromatic character of the triazole structure. The features at 400–450 nm correspond to water Raman bands observed in DI water blanks. Band intensity decreased with dilution, with detection appearing feasible in the 10-100 ppb range.

5.7 COMPARATIVE ANALYSIS OF PESTICIDE RESPONSE

The three pesticides tested produced markedly different detection outcomes. Zeta-cypermethrin showed the strongest fluorescence. It had emissions around 400-450 nm that stayed visible down to approximately 10 ppb and possibly 1 ppb. Glyphosate produced only weak and diffuse emission near 300-360 nm and was barely detectable at 1000 ppb and indistinguishable from baseline below 100 ppb. Myclobutanil is between these extremes, with UV-excited fluorescence around 280-290 nm excitation and 320-360 nm emission that provided detectability in the 10-100 ppb range.

The differences in intensity highlight how fluorescence intensity governs detectability in EEM measurements. Pesticides like zeta-cypermethrin generate robust emission above instrumental noise at the wavelengths tested. Compounds like glyphosate produce signals so weak they hit the lower bound of what the technique can measure without derivatization. The 60-second integration time used for these measurements is also a practical upper limit for field deployment and yet still could not push glyphosate above the detection threshold. Compounds such as myclobutanil provide a middle case. Where specific UV excitation wavelengths around 280-290 nm can be exploited to achieve detection in the 10-100 ppb range.

Noise ultimately determines these limits. At concentrations above 100 ppb, signal strength typically overcomes baseline variation from water Raman scattering and optical artifacts. Below 10 ppb, photon shot noise and baseline variability start to dominate the measurement. For weak emitters such as glyphosate, this noise floor obscures true signal even at 1000 ppb. For stronger emitters such as zeta-cypermethrin and myclobutanil, structured features stay distinguishable above the threshold down to approximately 10 ppb.

The wavelength separation between myclobutanil and zeta-cypermethrin suggests multi-analyte detection may be workable without advanced computation methods for compounds with little overlapping fluorescence signatures. This separation could be used in future sparse-band designs targeting specific pesticide combinations.

These results demonstrate that reagent-free EEM fluorescence works best for strongly fluorescent pesticides with extended conjugation, shows moderate effectiveness for compounds with distinct UV-excited signatures, and cannot detect weakly fluorescent molecules lacking aromatic character. These detection ranges establish which pesticide classes can be monitored with portable EEM systems and which require alternative approaches such as derivatization or LC-

MS/MS. These findings also provide experimental confirmation and revision for the detection limits predicted by the optical model in Chapter 4. Additionally, these findings will help identify which excitation–emission regions to prioritize for future sparse-band approaches.

Chapter 6. DISCUSSION, IMPLICATIONS, AND CONCLUSIONS

6.1 MODEL VS. REALITY: WHAT THE EXPERIMENTS REVEALED

The Chapter 3 radiometric model predicted sub-ppb detection limits for strongly fluorescent pesticides under idealized conditions. The experimental results told a different story. Zeta-cypermethrin and myclobutanil both achieved detection in the 10-100 ppb range. This is approximately one order of magnitude above the model's predictions. Glyphosate remained undetectable at all concentrations tested and confirmed the model's warnings about weakly fluorescent compounds but providing no path toward improvement.

This gap between prediction and reality reveals is where the idealized model broke down. The model used 30 mW optical output at UV wavelengths since this is around the highest optical power that commercial LEDs can achieve, but the actual benchtop system delivered only 1.6 mW at 290 nm and 0.33 mW at 341 nm due to part and time constraints. This represents an approximately 20-fold reduction in excitation power at the critical UV wavelengths where myclobutanil fluoresces. The visible LEDs performed better, delivering approximately 6 mW at 405 nm and 430 nm, but this was still 5 times lower than the modeled output and could be increased. Collection efficiency also suffered from imperfect alignment, use of fiber optic cables, and non-ideal optical components compared to the idealized assumptions. The Ocean Optics Flame spectrometer introduced a higher noise floor than the modeled Hamamatsu spectrometers. These losses compounded to reduce photon throughput compared to the idealized scenario.

The 60-second integration time used in these experiments represents another major deviation from the model's 1-second assumption. The longer exposure collected more photons but could not fully make up for the dramatically lower LED power outputs and other simplifying assumptions. This is a fundamental trade-off for portable devices. The longer integration times can improve sensitivity but can also reduce sampling throughput and increase power consumption. Field deployments would need to balance these constraints. They might need to accept higher/worse detection limits to maintain practical measurement speeds and to have a longer battery life.

Matrix effects also played a role in reducing sensitivity of the tests. Their contribution proved difficult to isolate. Baseline subtraction could not fully eliminate water Raman bands and optical artifacts in deionized water. The dissolved organic matter, suspended solids, and variable pH of real world environmental samples would push detection limits higher and continue to reduce sensitivity. The assumption of a clean, controlled matrix is likely not achievable in field measurements and are likely a best-case scenario.

Despite falling short of sub-ppb targets, the experimental results validated the core framework of Chapter 3's model. Compounds with strong fluorescence did produce detectable signals, and the relative detectability followed the prediction of the literature review. While the detection limits were significantly lower than what the model predicted, there are many improvements that can be made to the experiment to increase the threshold. The model successfully identified which pesticide classes are viable targets for reagent-free EEM detection. More importantly, the model's sensitivity to LED output power and integration time was validated:

the 20-fold reduction in UV power contributed directly to the observed order-of-magnitude shift in detection limits. These experiments confirmed the model's utility for system design and can help future iterations to target realistic specifications based on commercially available components rather than idealized values. Values will need to be tweaked and studied to continue to build an accurate model.

6.2 PRACTICAL IMPLICATIONS FOR PORTABLE EEM SYSTEMS

The experimental results are a start to establishing boundaries for what portable EEM systems can and cannot achieve with current technology. The 10-100 ppb detection range demonstrated for zeta-cypermethrin and myclobutanil sits approximately one order of magnitude above typical EPA aquatic-life benchmarks, however, through optimization and chemometric methods this is very achievable. This gap needs to be met and exceeded for regulatory compliance monitoring but may be acceptable for screening applications where rapid, reagent-free results can enable more frequent sampling than what current laboratory methods allow.

Reaching regulatory thresholds would require addressing the LED power limitation identified in Section 6.1, optimization of the current system, and the building of a prototype with chemometric process. All of this requires extensive study. Boosting UV output from 1.6 mW to 15-30 mW at 290 nm could push myclobutanil detection down toward 1-5 ppb and bring it within range of regulatory targets. Similarly, increasing visible LED power from 6 mW to 30-50 mW at 405-430 nm would improve zeta-cypermethrin sensitivity, however, more testing is needed for detection with different bands. Commercial deep-UV LEDs now deliver 10-20 mW at 280-290 nm in TO-can packages, though at significantly higher cost than the LEDs used in this study. The trade-off between detection limit and system cost will become a central design decision for field-deployable units in the near future.

Integration time is another critical constraint. The 60-second exposures used here enabled detection at 10-100 ppb but would limit field throughput to one sample per minute if doing only 1 band and not counting sample handling and data processing. In reality, each band needs to sampled independently. If the number of sample bands was increased to 6, this would result in a measurement time of at least 6 min for each sample. Reducing integration time to 10-15 seconds would greatly improve the practical utility but would likely push detection limits up to 50-200 ppb unless LED power and optical collection increased proportionally. These trade-offs must be evaluated against their intended use case. Some field screening applications might accept higher detection limits in exchange for faster throughput. However, compliance monitoring would likely still need sub-10 ppb sensitivity regardless of measurement speed.

Collection optics also warrant optimization. In these experiments, the benchtop system used basic lens assemblies that likely achieved 30-50% collection efficiency rather than the 70% assumed in the model. Custom-designed collection optics with higher numerical aperture and anti-reflection coatings could recover additional signal without increasing LED power or integration time and needs to be investigated. With new meta optics coming out, there is the possibility that almost all radiant power could be harvested. However, that seems to be quite distant and expensive. For a portable system, the best option is investing in high-quality UV-grade optics because this may prove to be more cost-effective than higher-power LEDs.

The wavelength separation between myclobutanil and zeta-cypermethrin does suggest multi-analyte detection may be feasible without complex chemometric deconvolution and processing. A new system with dedicated detection regions could monitor compounds without post processing. This approach would reduce the full EEM cube to critical excitation-emission regions and dramatically simplify data processing and enable faster acquisition. Future designs should and will probably prioritize non-overlapping spectral windows to maximize information content while minimizing hardware complexity and data processing.

Power consumption is a practical concern for battery-operated field units. The LEDs, spectrometer, and processing components would draw power during active measurement and while on standby. A field deployment that is running continuous measurements with 60-second integration would require battery capacity or solar supplementation to maintain multi-day operation. Reducing integration time to 15 seconds would reduce power consumption proportionally and could make it useable for extended field work.

6.3 LIMITATIONS AND FUTURE DIRECTIONS

This work makes three distinct contributions to portable pesticide sensing and portable EEM. First, the radiometric model developed in Chapter 3 connects component-level specifications to system-level detection limits, this was not present in other literature surveyed for pesticides. Future designs and systems can use this framework to predict performance based on commercially available LED power, collection efficiency, and detector noise characteristics without building physical prototypes. The model's sensitivity was experimentally validated and will be used to calibrate and refine future models.

Second, the experimental results show spectral discrimination between UV-excited and visible-excited pesticides without chromatographic separation. Myclobutanil fluoresced at 280-290 nm excitation while zeta-cypermethrin fluoresced under 405-430 nm excitation. Rather than creating full EEM cubes for each sample, this separation will enable sparse-band designs that target specific regions. In the end this reduces costs, power draw, and increases portability. Multi-analyte detection becomes much similar when compounds occupy non-overlapping spectral regions.

Third, this work is establishing quantitative boundaries for portable fluorescence detection and what compounds are feasible to test for. Strongly fluorescent pesticides achieved 10-100 ppb detection limits with basic optical components and relatively short integration times. Weakly fluorescent compounds like glyphosate produced no detectable signal at all tested levels, however, more testing is needed with chemometric methods. These boundaries will define what pesticide classes are viable targets with or without for detection in future work.

Portable EEM systems could monitor transient contamination events that are often missed with monthly sampling by enabling more frequent and lower-cost measurements. Pesticide pulses usually follow rainfall or irrigation and often exceed regulatory thresholds for hours to days before returning to baseline. In one application, these devices could identify when these events occur and trigger a confirmatory LC-MS/MS analysis. This could reduce cost or reinforce monitoring efforts.

Several fundamental limitations constrain broader applicability of future portable EEM devices. The restriction to fluorescent compounds is absolute. Glyphosate represents an entire class of pesticides that lack sufficient aromatic character to fluoresce detectably. EEM-based systems cannot be used as universal screening tools and must be used in conjunction with other systems. Chemical derivatization could extend coverage to non-fluorescent analytes but reintroduces reagent handling and preparation time.

All measurements used deionized water to isolated instrumental performance from environmental complexity. Surface runoff water contains random concentrations of dissolved organic matter, suspended solids, pH variations, and dissolved ions. These contaminants quench fluorescence, scatter light, or shift emission wavelengths during the sampling process. The 10-100 ppb detection limits demonstrated here will likely degrade in field samples as demonstrated in the model. Matrix validation is the most critical unaddressed variable.

The single-compound measurements in these tests is an extremely simplified version of field deployments. In practice, spectral overlap among pesticides will complicate separation and identification even when individual compounds are simple to detect. While myclobutanil and zeta-cypermethrin separated cleanly other pesticide combinations will not. Whether chemometric methods can reliably deconvolve overlapping signals under field-relevant conditions is still untested and will be studied under future work.

Temperature effects went unexplored. The benchtop system operated at room temperature between 22-24°C. Field measurements spanning 5-35°C would encounter temperature-dependent fluorescence changes requiring correction algorithms. LED stability over extended operation also requires investigation. In future field deployment, the system will need periodic recalibration to maintain consistent detection limits and up to date software.

6.4 FUTURE DIRECTIONS

Several research directions could extend the work of this thesis and prior work. Hardware improvements are one path forward. By using higher-power UV LEDs, the detection limits might be pushed lower. This would increase system cost however. Improved collection optics could recover additional signal without requiring more LED power. These upgrades would need to be evaluated to determine whether they provide sufficient sensitivity gains to justify added complexity and expense.

Two experimental validation gaps limit the understanding of real-world performance. First, all measurements here used deionized water to isolate instrumental performance. During field work, environmental samples contain random contaminants that could degrade sensitivity. In future work, the detection limits will need to be tested with river water, agricultural runoff, and tap water samples. This work will establish whether the 10-100 ppb range is relevant under field-relevant conditions. Second, mixing pesticides together would clarify whether spectral overlap prevents simultaneous detection of multiple pesticides. The clean wavelength separation between myclobutanil and zeta-cypermethrin suggests multi-analyte detection may be feasible, but testing this with commonly co-occurring pesticides is needed to verify this. With these studies, portable EEM would be feasible beyond single-compound measurements in clean matrices.

Computational analysis of the existing EEM data could identify minimal excitation-emission pairs needed for compound discrimination. A sparse-band approach with fewer wavelength bands might reduce acquisition time while maintaining analytical capability. Though this optimization has not been attempted and requires multiple rounds of testing. These directions represent natural extensions of the work presented here, though each requires additional experimental effort and resources to pursue.

6.5 CONCLUDING REMARKS

This thesis set out to determine whether excitation–emission matrix fluorescence could detect pesticides at concentrations relevant to environmental monitoring using portable, low-cost hardware. The answer is not a simple yes or no. For strongly fluorescent pesticides like zeta-cypermethrin and myclobutanil, portable EEM technique works. Detection limits of 10-100 ppb were achieved using commercially available components with little modification. This means portable EEM systems are within one order of magnitude of regulatory thresholds and with a dramatically lower cost per sample than laboratory LC-MS/MS. The gap between current performance and regulatory requirements appears to be closable with hardware upgrades. This can done either with higher-power UV LEDs and improved collection optics. Reagent-free EEM cannot provide detection at any relevant concentration without additional analysis and processing for weakly fluorescent compounds like glyphosate. This fundamental limitation stems from photophysics of the pesticide and not instrumentation. No increase of LED power or integration time will make non-fluorescent pesticides detectable without chemical derivatization.

The radiometric model developed here successfully predicted which pesticide classes would be detectable based on reviewed quantum yields and identified multiple limiting factor. While the model overestimated its absolute sensitivity due to idealized LED power assumptions and simplified collection efficiency, this model provides a validated framework for future system designs. The model also assumed monochromatic excitation and emission, treating LEDs as narrow spectral lines rather than the 10-15 nm bandwidth sources they actually are. This simplification meant the model does not account for how emitted photons are distributed across wavelengths when pesticides are excited. Despite these idealizations, the model connects component specifications to achievable detection limits without requiring iterative prototyping. This will enable accelerated development cycles for portable fluorescence instruments with improved understanding of the photo physic properties of pesticides. More importantly, the experimental validation confirmed the model's core predictions. Photon throughput governs detection limits, and strongly fluorescent compounds provide sufficient signal margins to overcome instrumental noise. The 20x reduction in actual LED power compared to modeled values produced a corresponding order-of-magnitude shift in detection limits which can be explained in the model's sensitivity analysis. The 60-second integration time used in experiments partially compensated for lower LED power by collecting photons over longer periods, though this compensation proved incomplete as detector noise also accumulated over time.

Portable EEM systems can occupy a specific niche in pesticide monitoring. They complement rather than replace laboratory methods. Their value is from their ability in enabling frequent, low-cost screening that can identify contamination events or track temporal trends. This can augment laboratory confirmation and highlight when samples exceed threshold concentrations or for compounds outside the technique's fluorescence-based scope for in lab testing. By using portable EEM monitoring in tiered monitoring approaches, these systems could increase sampling frequency while managing costs and potentially catching transient contamination pulses following rainfall or irrigation that monthly sampling misses entirely. The work presented here is starting to establish both capabilities and boundaries of these system. This works hopes it demonstrates that portable fluorescence detection can achieve meaningful sensitivity for certain pesticide classes while acknowledging the limitations. These boundaries define the foundation upon which future portable monitoring systems can be built and will continue to clarify which pesticide classes warrant continued development effort and which require alternative analytical approaches.

Bibliography

[1] S. M. Stackpoole, M. E. Shoda, L. Medalie, and W. W. Stone, "Pesticides in US Rivers: Regional differences in use, occurrence, and environmental toxicity, 2013 to 2017," *Science of The Total Environment,* vol. 787, p. 147147, 2021/09/15/ 2021, doi: https://doi.org/10.1016/j.scitotenv.2021.147147.

[2] R. Budd, "Surface Water Ambient Monitoring Report," California Department of Pesticide Regulation, 2025. [Online]. Available: https://www.cdpr.ca.gov/wp-content/uploads/2025/07/Study-320-Ambient-Monitoring-Report_WY23_24.pdf

[3] S. Singh, S. Sharma, S. J. Sarma, K. Misra, and S. K. Brar, "Chapter 10 - Pesticides in water," in *Handbook of Water Purity and Quality (Second Edition)*, S. Ahuja Ed. Amsterdam: Academic Press, 2021, pp. 231-253.

[4] D. Atwood and C. Paisley-Jones, "Pesticides Industry Sales and Usage," U.S. Environmental Protection Agency, 2017. [Online]. Available: https://www.epa.gov/sites/default/files/2017-01/documents/pesticides-industry-sales-usage-2016_0.pdf

[5] C. M. Wieben. *Estimated annual agricultural pesticide use by major crop or crop group for states of the conterminous United States, 1992-2019 (including preliminary estimates for 2018-19)*, U.S. Geological Survey, doi: 10.5066/P900FZ6Y.

[6] S. J. Larson, R. J. Gilliom, and P. D. Capel, *Pesticides in streams of the United States: initial results from the national water-quality assessment program*. US Department of the Interior, US Geological Survey, 1999.

[7] "National Primary Drinking Water Regulations." US Environmental Protection Agency. https://www.epa.gov/ground-water-and-drinking-water/national-primary-drinking-water-regulations (accessed June 13th, 2025).

[8] "EPA Updates Aquatic Life Benchmarks for Registered Conventional and Antimicrobial Pesticides." US Environmental Protection Agency. https://www.epa.gov/pesticides/epa-updates-aquatic-life-benchmarks-registered-conventional-and-antimicrobial-pesticides (accessed June 13th, 2025).

[9] "2021 Human Health Benchmarks for Pesticides." US Environmental Protection Agency. https://www.epa.gov/sdwa/human-health-benchmarks (accessed June 13th, 2025).

[10] J. Cotruvo *et al.*, "Background Document for Development of WHO Guidelines for Drinking Water Quality," Report WHO/HSE/WSH/10.01/Rev1 Hardness in Drinking Water, Geneva, Switzerland, 2011.

[11] D. Main. "New data show widespread chemical contamination of drinking water." The New Lede. https://www.thenewlede.org/2025/02/new-data-widespread-chemical-contamination-drinking-water/ (accessed July 15th, 2025).

[12] C. Liang *et al.*, "Pesticide Residue Monitoring Program Fiscal Year 2022 Pesticide Report ", 2024. [Online]. Available: https://www.fda.gov/media/181381/download?attachment#page=4.07

[13] J. Xue *et al.*, "Portable sensors equipped with smartphones for organophosphorus pesticides detection," *Food Chemistry,* vol. 434, p. 137456, 2024/02/15/ 2024, doi: https://doi.org/10.1016/j.foodchem.2023.137456.

[14] M. Park and S. A. Snyder, "Sample handling and data processing for fluorescent excitation-emission matrix (EEM) of dissolved organic matter (DOM)," *Chemosphere,* vol. 193, pp. 530-537, 2018/02/01/ 2018, doi: https://doi.org/10.1016/j.chemosphere.2017.11.069.

[15] G. J. Hall and J. E. Kenny, "Estuarine water classification using EEM spectroscopy and PARAFAC–SIMCA," *Analytica Chimica Acta,* vol. 581, no. 1, pp. 118-124, 2007/01/02/ 2007, doi: https://doi.org/10.1016/j.aca.2006.08.034.

[16] D. Omanović, S. Marcinek, and C. Santinelli, "TreatEEM—A Software Tool for the Interpretation of Fluorescence Excitation-Emission Matrices (EEMs) of Dissolved Organic Matter in Natural Waters," *Water*, vol. 15, no. 12*,* doi: 10.3390/w15122214.

[17] R. D. JiJi, G. A. Cooper, and K. S. Booksh, "Excitation-emission matrix fluorescence based determination of carbamate pesticides and polycyclic aromatic hydrocarbons," *Analytica chimica acta,* vol. 397, no. 1-3, pp. 61-72, 1999.

[18] M. Tedetti, P. Joffre, and M. Goutx, "Development of a field-portable fluorometer based on deep ultraviolet LEDs for the detection of phenanthrene- and tryptophan-like compounds in natural waters," *Sensors and Actuators B: Chemical,* vol. 182, pp. 416-423, 2013/06/01/ 2013, doi: https://doi.org/10.1016/j.snb.2013.03.052.

[19] A. Jechow *et al.*, "Characterizing and Implementing the Hamamatsu C12880MA Mini-Spectrometer for Near-Surface Reflectance Measurements of Inland Waters," *Sensors*, vol. 24, no. 19*,* doi: 10.3390/s24196445.

[20] G. López-Pérez, D. González-Arjona, E. Roldán González, and C. Román-Hidalgo, "Design of a Portable and Reliable Fluorimeter with High Sensitivity for Molecule Trace Analysis," *Chemosensors*, vol. 11, no. 7*,* doi: 10.3390/chemosensors11070389.

[21] Z. Guo *et al.*, "Detection of pesticide in water using two-dimensional fluorescence correlation spectroscopy and N-way partial least squares," *Spectrochimica Acta Part A: Molecular and Biomolecular Spectroscopy,* vol. 229, p. 117981, 2020/03/15/ 2020, doi: https://doi.org/10.1016/j.saa.2019.117981.

[22] M. Levine, "Fluorescence-Based Sensing of Pesticides Using Supramolecular Chemistry," (in eng), *Front Chem,* vol. 9, p. 616815, 2021, doi: 10.3389/fchem.2021.616815.

[23] W. Lei, Z. Gu, W. Si, F. Wang, and Q. Hao, "Fluorescent poly (2, 6-dimethoxynaphthalene) electrochemically synthesized for sensitive detection of imidacloprid pesticide," *Journal of The Electrochemical Society,* vol. 160, no. 8, p. H502, 2013.

[24] H. Chang, H. Wu, T. Wang, X. Wang, and R. Yu, "Multi-Way Fluorescence Technique Combined with Four-Way Calibration for the Determination of Thiabendazole and Carbaryl in Apple," *Chemosensors*, vol. 13, no. 3*,* doi: 10.3390/chemosensors13030107.

[25] B. Englert, "Method 1699: Pesticides in water, soil, sediment, biosolids, and tissue by HRGC/HRMS," *US Environmental Protection Agency (EPA),* pp. 1-96, 2007.

[26] J. Moriceau *et al.*, "An advanced integrated GC-MS/MS and LC-MS/MS workflow for the comprehensive analysis of pesticide residues in food ", ed: ThermoFisher Scientific, 2024.

[27] "Pesticide Multi-Residue Analysis (MRA) - Basic Screen." Medallion Labs. https://www.medallionlabs.com/tests/pesticide-multi-residue-analysis-basic-screen/ (accessed July 17th, 2025).

[28] A. A. A. Radowan, "Analytical techniques for determining pesticide residues in food: A comprehensive review," *International Journal of Materials Technology and Innovation,* vol. 4, no. 1, pp. 42-74, 2024.

[29] M. Xiao *et al.*, "A smartphone-based fluorospectrophotometer and ratiometric fluorescence nanoprobe for on-site quantitation of pesticide residue," *iScience,* vol. 26, no. 4, p. 106553, 2023/04/21/ 2023, doi: https://doi.org/10.1016/j.isci.2023.106553.
[30] S. Stackpoole, "Assessing Pesticide Use, Stream Concentrations, and Health Criteria," ed: U.S. Geological Survey, 2021.
[31] S. Links, "Occurrence and Distribution of Pesticides in Surface Waters of the Hood River Basin, Oregon, 1999–2009."
[32] R. C. Gore, R. W. Hannah, S. C. Pattacini, and T. J. Porro, "Infrared and ultraviolet spectra of seventy-six pesticides," 1971.
[33] H. U. Okoroiwu and I. A. Iwara, "Dichlorvos toxicity: A public health perspective," (in eng), *Interdiscip Toxicol,* vol. 11, no. 2, pp. 129-137, Aug 2018, doi: 10.2478/intox-2018-0009.
[34] J. Wu, X. Chen, Z. Zhang, and J. Zhang, "“Off-on” fluorescence probe based on green emissive carbon dots for the determination of Cu2+ ions and glyphosate and development of a smart sensing film for vegetable packaging," *Microchimica Acta,* vol. 189, no. 3, p. 131, 2022/03/03 2022, doi: 10.1007/s00604-022-05241-5.
[35] H. W. Chu, B. Unnikrishnan, A. Anand, Y. W. Lin, and C. C. Huang, "Carbon quantum dots for the detection of antibiotics and pesticides," (in eng), *J Food Drug Anal,* vol. 28, no. 4, pp. 539-557, Dec 15 2020, doi: 10.38212/2224-6614.1269.
[36] Z. Zhang, Q. Zhang, L. Li, D. Lin, and C. Jiang, "Ultrasensitive and On-Site Detection of Carbaryl Pesticides via Dual-Mode Nanosensors Utilizing Portable Devices," *ACS Sustainable Chemistry & Engineering,* vol. 11, no. 13, pp. 4998-5006, 2023/04/03 2023, doi: 10.1021/acssuschemeng.2c06499.
[37] J. Du, H. Wu, X. Jing, Y. Yu, Z. Yan, and J. Zhang, "Development of a Sensitive and Fast Determination Method for Trace Carbaryl Residues in Food Samples Based on Magnetic COF (TpPa-NH2)@Fe3O4 Nanoparticles and Fluorescence Detection," *Foods*, vol. 11, no. 19*,* doi: 10.3390/foods11193130.
[38] A. Asghar, D. Lipfert, K. Kerpen, and T. C. Schmidt, "Elucidating the inhibitory effects of natural organic matter on the photodegradation of organic micropollutants: Atrazine as a probe compound," *Chemosphere,* vol. 352, p. 141390, 2024/03/01/ 2024, doi: https://doi.org/10.1016/j.chemosphere.2024.141390.
[39] J. Dai and M. Fidalgo de Cortalezzi, "Influence of pH, ionic strength and natural organic matter concentration on a MIP-Fluorescent sensor for the quantification of DNT in water," *Heliyon,* vol. 5, no. 6, 2019/6 2019, doi: 10.1016/j.heliyon.2019.e01922.
[40] Y. Xu *et al.*, "Photochemical behavior of dissolved organic matter in environmental surface waters: A review," (in eng), *Eco Environ Health,* vol. 3, no. 4, pp. 529-542, Dec 2024, doi: 10.1016/j.eehl.2024.06.002.
[41] Z.-H. Wang, Z.-P. Zhang, Z.-P. Wang, L.-W. Liu, and X.-P. Yan, "Acrylic acid grafted polytetrafluoroethylene fiber as new packing for flow injection on-line microcolumn preconcentration coupled with flame atomic absorption spectrometry for determination of lead and cadmium in environmental and biological samples," *Analytica Chimica Acta,* vol. 514, no. 2, pp. 151-157, 2004/07/01/ 2004, doi: https://doi.org/10.1016/j.aca.2004.03.049.
[42] M. Catalá-Icardo, S. Meseguer-Lloret, and S. Torres-Cartas, "Photoinduced chemiluminescence determination of carbamate pesticides," *Photochemical &*

Photobiological Sciences, vol. 15, no. 5, pp. 626-634, 2016/05/01 2016, doi: 10.1039/c6pp00056h.

[43] T. López-López, M. D. Gil-Garcia, J. L. Martínez-Vidal, and M. Martínez-Galera, "Determination of pyrethroids in vegetables by HPLC using continuous on-line post-elution photoirradiation with fluorescence detection," *Analytica Chimica Acta,* vol. 447, no. 1, pp. 101-111, 2001/11/26/ 2001, doi: https://doi.org/10.1016/S0003-2670(01)01305-8.

[44] F. Ou, C. McGoverin, S. Swift, and F. Vanholsbeeck, "Rapid and cost-effective evaluation of bacterial viability using fluorescence spectroscopy," *Analytical and Bioanalytical Chemistry,* vol. 411, no. 16, pp. 3653-3663, 2019/06/01 2019, doi: 10.1007/s00216-019-01848-5.

[45] G. Mahamuni *et al.*, "Solid-phase excitation-emission matrix spectroscopy for chemical analysis of combustion aerosols," *PLOS ONE,* vol. 16, no. 5, p. e0251664, 2021, doi: 10.1371/journal.pone.0251664.

[46] D. E. Zacharioudaki, I. Fitilis, and M. Kotti, "Review of Fluorescence Spectroscopy in Environmental Quality Applications," (in eng), *Molecules,* vol. 27, no. 15, Jul 27 2022, doi: 10.3390/molecules27154801.

[47] A. Surampudi, A. Aryal, T. Hewagama, N. Prasad, D. M. Bower, and M. C. Gupta, "Mixture Detection Using a Deep-UV Raman-LIBS Autofocus-Based Compact Chemical Spectroscopic Sensor," (in eng), *ACS Omega,* vol. 10, no. 30, pp. 33471-33480, Aug 5 2025, doi: 10.1021/acsomega.5c03801.

[48] M. Kumar, K. Khamis, R. Stevens, D. M. Hannah, and C. Bradley, "In-situ optical water quality monitoring sensors—applications, challenges, and future opportunities," *Frontiers in Water,* Review vol. Volume 6 - 2024, 2024.

[49] M. Kneissl *et al.*, "Advances in group III-nitride-based deep UV light-emitting diode technology," *Semiconductor Science and Technology,* vol. 26, no. 1, p. 014036, 2010/12/15 2011, doi: 10.1088/0268-1242/26/1/014036.

[50] M. Shatalov *et al.*, "AlGaN Deep-Ultraviolet Light-Emitting Diodes with External Quantum Efficiency above 10%," *Applied Physics Express,* vol. 5, no. 8, p. 082101, 2012/07/11 2012, doi: 10.1143/APEX.5.082101.

[51] M. Kneissl, T.-Y. Seong, J. Han, and H. Amano, "The emergence and prospects of deep-ultraviolet light-emitting diode technologies," *Nature Photonics,* vol. 13, no. 4, pp. 233-244, 2019/04/01 2019, doi: 10.1038/s41566-019-0359-9.

[52] Y. Nagasawa and A. Hirano, "A Review of AlGaN-Based Deep-Ultraviolet Light-Emitting Diodes on Sapphire," *Applied Sciences*, vol. 8, no. 8*,* doi: 10.3390/app8081264.

[53] C.-Y. Kang, C.-H. Lin, T. Wu, P.-T. Lee, Z. Chen, and H.-C. Kuo, "A novel liquid packaging structure of deep-ultraviolet light-emitting diodes to enhance the light-extraction efficiency," *Crystals,* vol. 9, no. 4, p. 203, 2019.

[54] J. Juola, "Prototyping electronics and software for a spectrometer module," 2017.

[55] O. Hotra, V. Firago, N. Levkovich, and K. Shuliko, "Investigation of the Possibility of Using Microspectrometers Based on CMOS Photodiode Arrays in Small-Sized Devices for Optical Diagnostics," (in eng), *Sensors (Basel),* vol. 22, no. 11, May 31 2022, doi: 10.3390/s22114195.

[56] M. J. M. Wells, J. Hooper, G. A. Mullins, and K. Y. Bell, "Development of a fluorescence EEM-PARAFAC model for potable water reuse monitoring: Implications for inter-

component protein–fulvic–humic interactions," *Science of The Total Environment,* vol. 820, p. 153070, 2022/05/10/ 2022, doi: https://doi.org/10.1016/j.scitotenv.2022.153070.

[57] A. J. Lawaetz and C. A. Stedmon, "Fluorescence intensity calibration using the Raman scatter peak of water," (in eng), *Appl Spectrosc,* vol. 63, no. 8, pp. 936-40, Aug 2009, doi: 10.1366/000370209788964548.

[58] A. J. Harvie, S. K. Yadav, and J. C. de Mello, "A sensitive and compact optical detector based on digital lock-in amplification," *HardwareX,* vol. 10, 2021, doi: 10.1016/j.ohx.2021.e00228.

[59] F. Pollastrone, L. Fiorani, R. Bisauriya, I. Menicucci, C. Ciceroni, and R. Pizzoferrato, "Development and Test of Low-Cost Multi-Channel Multi-Frequency Lock-In Amplifier for Health and Environment Sensing," *Sensors*, vol. 24, no. 18, doi: 10.3390/s24186020.

[60] H. Wang, Y. Qi, T. J. Mountziaris, and C. D. Salthouse, "A portable time-domain LED fluorimeter for nanosecond fluorescence lifetime measurements," *Review of Scientific Instruments,* vol. 85, no. 5, p. 055003, 2014, doi: 10.1063/1.4873330.

[61] P. C. DeRose, *Standard guide to fluorescence: Instrument calibration and validation*. US Department of Commerce, Technology Admininstration, National Institute of …, 2007.

[62] H. Lemmetyinen *et al.*, "Time-resolved fluorescence methods (IUPAC Technical Report)," vol. 86, no. 12, pp. 1969-1998, 2014, doi: doi:10.1515/pac-2013-0912.

[63] G. M. Foster *et al.*, "Field techniques for the determination of algal pigment fluorescence in environmental waters—Principles and guidelines for instrument and sensor selection, operation, quality assurance, and data reporting," US Geological Survey, 2328-7055, 2022.

[64] Y. B. Ma and J. K. Amamcharla, "A rapid method to quantify casein in fluid milk by front-face fluorescence spectroscopy combined with chemometrics," (in eng), *J Dairy Sci,* vol. 104, no. 1, pp. 243-252, Jan 2021, doi: 10.3168/jds.2020-18799.

[65] L. Latchoumane *et al.*, "Front-Face Fluorescence Spectroscopy and Feature Selection for Fruit Classification Based on N-CovSel Method," *Frontiers in Analytical Science,* Original Research vol. Volume 2 - 2022, 2022.

[66] A. T. Taylor and E. P. C. Lai, "Current State of Laser-Induced Fluorescence Spectroscopy for Designing Biochemical Sensors," *Chemosensors*, vol. 9, no. 10, doi: 10.3390/chemosensors9100275.

[67] G. Ryu *et al.*, "Highly sensitive fluorescence detection system for microfluidic lab-on-a-chip," *Lab on a Chip,* 10.1039/C0LC00586J vol. 11, no. 9, pp. 1664-1670, 2011, doi: 10.1039/C0LC00586J.

[68] C. Würth, J. Pauli, C. Lochmann, M. Spieles, and U. Resch-Genger, "Integrating Sphere Setup for the Traceable Measurement of Absolute Photoluminescence Quantum Yields in the Near Infrared," *Analytical Chemistry,* vol. 84, no. 3, pp. 1345-1352, 2012/02/07 2012, doi: 10.1021/ac2021954.

[69] T. Weitner, T. Friganović, and D. Šakić, "Inner Filter Effect Correction for Fluorescence Measurements in Microplates Using Variable Vertical Axis Focus," (in eng), *Anal Chem,* vol. 94, no. 19, pp. 7107-7114, May 17 2022, doi: 10.1021/acs.analchem.2c01031.

[70] J. Kimball *et al.*, "On the origin and correction for inner filter effects in fluorescence Part I: primary inner filter effect-the proper approach for sample absorbance correction," (in eng), *Methods Appl Fluoresc,* vol. 8, no. 3, p. 033002, Jun 1 2020, doi: 10.1088/2050-6120/ab947c.

[71] R. M. Cory, M. P. Miller, D. M. McKnight, J. J. Guerard, and P. L. Miller, "Effect of instrument-specific response on the analysis of fulvic acid fluorescence spectra," *Limnology and Oceanography: Methods,* vol. 8, no. 2, pp. 67-78, 2010/02/01 2010, doi: https://doi.org/10.4319/lom.2010.8.67.

[72] D. N. Kothawala, K. R. Murphy, C. A. Stedmon, G. A. Weyhenmeyer, and L. J. Tranvik, "Inner filter correction of dissolved organic matter fluorescence," *Limnology and Oceanography: Methods,* vol. 11, no. 12, pp. 616-630, 2013/12/01 2013, doi: https://doi.org/10.4319/lom.2013.11.616.

[73] J. A. Korak and G. McKay, "Critical review of fluorescence and absorbance measurements as surrogates for the molecular weight and aromaticity of dissolved organic matter," *Environmental Science: Processes & Impacts,* vol. 26, no. 10, pp. 1663-1702, 2024.

[74] C. A. Stedmon and R. Bro, "Characterizing dissolved organic matter fluorescence with parallel factor analysis: a tutorial," *Limnology and Oceanography: Methods,* vol. 6, no. 11, pp. 572-579, 2008/11/01 2008, doi: https://doi.org/10.4319/lom.2008.6.572.

[75] C. M. Andersen and R. Bro, "Practical aspects of PARAFAC modeling of fluorescence excitation-emission data," *Journal of Chemometrics,* vol. 17, no. 4, pp. 200-215, 2003/04/01 2003, doi: https://doi.org/10.1002/cem.790.

[76] K. R. Murphy, C. A. Stedmon, D. Graeber, and R. Bro, "Fluorescence spectroscopy and multi-way techniques. PARAFAC," *Analytical Methods,* 10.1039/C3AY41160E vol. 5, no. 23, pp. 6557-6566, 2013, doi: 10.1039/C3AY41160E.

[77] A. C. Olivieri, J. A. Arancibia, A. Muñoz de la Peña, I. Durán-Merás, and A. Espinosa Mansilla, "Second-order advantage achieved with four-way fluorescence excitation-emission-kinetic data processed by parallel factor analysis and trilinear least-squares. Determination of methotrexate and leucovorin in human urine," (in eng), *Anal Chem,* vol. 76, no. 19, pp. 5657-66, Oct 1 2004, doi: 10.1021/ac0493065.

[78] A. C. Olivieri, "On a versatile second-order multivariate calibration method based on partial least-squares and residual bilinearization: Second-order advantage and precision properties," *Journal of Chemometrics,* vol. 19, no. 4, pp. 253-265, 2005/04/01 2005, doi: https://doi.org/10.1002/cem.927.

[79] R. Bro, "Multiway calibration. Multilinear PLS," *Journal of Chemometrics,* vol. 10, no. 1, pp. 47-61, 1996/01/01 1996, doi: https://doi.org/10.1002/(SICI)1099-128X(199601)10:1<47::AID-CEM400>3.0.CO;2-C.

[80] N. M. Faber and R. Bro, "Standard error of prediction for multiway PLS: 1. Background and a simulation study," *Chemometrics and Intelligent Laboratory Systems,* vol. 61, no. 1, pp. 133-149, 2002/02/28/ 2002, doi: https://doi.org/10.1016/S0169-7439(01)00204-0.

[81] N. M. Peleato, R. L. Legge, and R. C. Andrews, "Neural networks for dimensionality reduction of fluorescence spectra and prediction of drinking water disinfection by-products," (in eng), *Water Res,* vol. 136, pp. 84-94, Jun 1 2018, doi: 10.1016/j.watres.2018.02.052.

[82] N. M. Peleato, "Application of convolutional neural networks for prediction of disinfection by-products," (in eng), *Sci Rep,* vol. 12, no. 1, p. 612, Jan 12 2022, doi: 10.1038/s41598-021-03881-w.

[83] M. Pucher, U. Wünsch, G. Weigelhofer, K. Murphy, T. Hein, and D. Graeber, "staRdom: Versatile Software for Analyzing Spectroscopic Data of Dissolved Organic Matter in R," *Water*, vol. 11, no. 11*,* doi: 10.3390/w11112366.

[84] Q. Sun *et al.*, "A review on recent advances in mass spectrometry analysis of harmful contaminants in food," (in eng), *Front Nutr,* vol. 10, p. 1244459, 2023, doi: 10.3389/fnut.2023.1244459.

[85] M. Anastassiades, S. J. Lehotay, D. Štajnbaher, and F. J. Schenck, "Fast and Easy Multiresidue Method Employing Acetonitrile Extraction/Partitioning and “Dispersive Solid-Phase Extraction” for the Determination of Pesticide Residues in Produce," *Journal of AOAC INTERNATIONAL,* vol. 86, no. 2, pp. 412-431, 2003, doi: 10.1093/jaoac/86.2.412.

[86] T. Pihlström *et al.*, "Analytical quality control and method validation procedures for pesticide residues analysis in food and feed SANTE 11312/2021," *Sante,* vol. 11312, no. v2, 2021.

[87] M. D. L. Jara, L. A. C. Alvarez, M. C. C. Guimarães, P. W. P. Antunes, and J. P. de Oliveira, "Lateral flow assay applied to pesticides detection: recent trends and progress," *Environmental Science and Pollution Research,* vol. 29, no. 31, pp. 46487-46508, 2022/07/01 2022, doi: 10.1007/s11356-022-20426-4.

[88] R. Zou *et al.*, "Up-Converting Nanoparticle-Based Immunochromatographic Strip for Multi-Residue Detection of Three Organophosphorus Pesticides in Food," *Frontiers in Chemistry,* Original Research vol. Volume 7 - 2019, 2019.

[89] T. O. Hara and B. Singh, "Electrochemical Biosensors for Detection of Pesticides and Heavy Metal Toxicants in Water: Recent Trends and Progress," *ACS ES&T Water,* vol. 1, no. 3, pp. 462-478, 2021/03/12 2021, doi: 10.1021/acsestwater.0c00125.

[90] J. Cao *et al.*, "An Overview on the Mechanisms and Applications of Enzyme Inhibition-Based Methods for Determination of Organophosphate and Carbamate Pesticides," *Journal of Agricultural and Food Chemistry,* vol. 68, no. 28, pp. 7298-7315, 2020/07/15 2020, doi: 10.1021/acs.jafc.0c01962.

[91] Z. Gong, Y. Huang, X. Hu, J. Zhang, Q. Chen, and H. Chen, "Recent Progress in Electrochemical Nano-Biosensors for Detection of Pesticides and Mycotoxins in Foods," *Biosensors*, vol. 13, no. 1, doi: 10.3390/bios13010140.

[92] E. Piskin, Z. Alakus, F. Budak, A. Cetinkaya, and S. A. Ozkan, "Nanoparticle-supported electrochemical sensors for pesticide analysis in fruit juices," *Journal of Pharmaceutical and Biomedical Analysis Open,* vol. 5, p. 100056, 2025/06/01/ 2025, doi: https://doi.org/10.1016/j.jpbao.2025.100056.

[93] B. Y. Chu, C. Lin, P. C. Nie, and Z. Y. Xia, "Research Status in the Use of Surface-Enhanced Raman Scattering (SERS) to Detect Pesticide Residues in Foods and Plant-Derived Chinese Herbal Medicines," (in eng), *Int J Anal Chem,* vol. 2024, p. 5531430, 2024, doi: 10.1155/2024/5531430.

[94] L. Jiang, M. M. Hassan, S. Ali, H. Li, R. Sheng, and Q. Chen, "Evolving trends in SERS-based techniques for food quality and safety: A review," *Trends in Food Science & Technology,* vol. 112, pp. 225-240, 2021/06/01/ 2021, doi: https://doi.org/10.1016/j.tifs.2021.04.006.

[95] Z. Jiang, Y. Zhuang, S. Guo, A. S. M. M. F. Sohan, and B. Yin, "Advances in Microfluidics Techniques for Rapid Detection of Pesticide Residues in Food," *Foods*, vol. 12, no. 15, doi: 10.3390/foods12152868.

[96] S. Das, Gagandeep, and R. Bhatia, "Paper-based microfluidic devices: Fabrication, detection, and significant applications in various fields," vol. 41, no. 1, pp. 112-136, 2022, doi: doi:10.1515/revac-2022-0037.

[97] D. Duff *et al.*, "Portable gas chromatography-mass spectrometry method for the in-field screening of organic pollutants in soil and water at pollution incidents," (in eng), *Environ Sci Pollut Res Int,* vol. 30, no. 40, pp. 93088-93102, Aug 2023, doi: 10.1007/s11356-023-28648-w.

[98] J. Wang, M. E. Pursell, A. DeVor, O. Awoyemi, S. J. Valentine, and P. Li, "Portable mass spectrometry system: instrumentation, applications, and path to 'omics analysis," (in eng), *Proteomics,* vol. 22, no. 23-24, p. e2200112, Dec 2022, doi: 10.1002/pmic.202200112.

[99] S. Rankin-Turner, J. C. Reynolds, M. A. Turner, and L. M. Heaney, "Applications of ambient ionization mass spectrometry in 2021: An annual review," *Analytical Science Advances,* vol. 3, no. 3-4, pp. 67-89, 2022/04/01 2022, doi: https://doi.org/10.1002/ansa.202100067.

[100] J. R. Lakowicz, *Principles of fluorescence spectroscopy*. Springer, 2006.

[101] D. P. Zamora, M. M. Galera, A. G. Frenich, and J. L. M. Vidal, "Trace determination of carbendazim, fuberidazole and thiabendazole in water by application of multivariate calibration to cross-sections of three-dimensional excitation–emission matrix fluorescence," *Analyst,* 10.1039/A909886K vol. 125, no. 6, pp. 1167-1174, 2000, doi: 10.1039/A909886K.

[102] M. J. Rodrıguez-Cuesta, R. Boqué, F. X. Rius, D. P. Zamora, M. M. Galera, and A. G. Frenich, "Determination of carbendazim, fuberidazole and thiabendazole by three-dimensional excitation–emission matrix fluorescence and parallel factor analysis," *Analytica Chimica Acta,* vol. 491, no. 1, pp. 47-56, 2003.

[103] S.-H. Zhu *et al.*, "Determination of pesticides in honey using excitation–emission matrix fluorescence coupled with second-order calibration and second-order standard addition methods," *Analytica Chimica Acta,* vol. 619, no. 2, pp. 165-172, 2008/07/07/ 2008, doi: https://doi.org/10.1016/j.aca.2008.05.005.

[104] D. C. Harris, *Quantitative chemical analysis*. Macmillan, 2010.

[105] M. Strojnik and M. K. Scholl, "Radiometry," in *Advanced optical instruments and techniques*: CRC Press, 2017, pp. 459-516.

[106] "NVSU233BT," 2017. [Online]. Available: https://www.us.lumistrips.com/amfile/file/download/file/1380/product/5707/

[107] M. Maraj, L. Min, and W. Sun, "Reliability Analysis of AlGaN-Based Deep UV-LEDs," *Nanomaterials*, vol. 12, no. 21, doi: 10.3390/nano12213731.

[108] "UV Fused Silica Plano-Convex Lenses, Uncoated." Thorlabs, Inc. https://www.thorlabs.com/newgrouppage9.cfm?objectgroup_id=123 (accessed September 4th, 2025).

[109] "Mini-spectrometers," 2025. [Online]. Available: https://www.hamamatsu.com/content/dam/hamamatsu-photonics/sites/documents/99_SALES_LIBRARY/ssd/c12880ma_c16767ma_kacc1226e.pdf

[110] R. Li, J. Dong, G. Wu, L. Gao, and M. Yang, "A novel turbidity compensation method for fluorescence spectroscopy and application in the detection of two algae species,"

Spectrochimica Acta Part A: Molecular and Biomolecular Spectroscopy, vol. 329, p. 125510, 2025/03/15/ 2025, doi: https://doi.org/10.1016/j.saa.2024.125510.